Reaching a Burning Plasma and Ignition Using Smaller Capsules/Hohlraums, Higher Radiation Temperatures and Thicker Ablator/Ice on the National Ignition Facility

K. L. Baker[a], C. A. Thomas, O. L. Landen, S. Haan, J.D. Lindl, D. T. Casey, C. Young, R. Nora, O.A. Hurricane, D.A. Callahan, O. Jones, L. Berzak Hopkins, S. Khan, B. K. Spears, S. Le Pape, N. B. Meezan, D. D. Ho, T. Döppner, D. Hinkel, E. L. Dewald, R. Tommasini, M. Hohenberger, C. Weber, D. Clark, D. T. Woods, J. L. Milovich, D. Strozzi, A. Kritcher, H. F. Robey, J. S. Ross, V. S. Smalyuk, P. A. Amendt, B. Bachmann, L. R. Benedetti, R. Bionta, P.M. Celliers, D. Fittinghoff, C. Goyon, R. Hatarik, N. Izumi, M. Gatu Johnson, G. Kyrala, T. Ma, K. Meaney, M. Millot, S. R. Nagel, P. K. Patel, D. Turnbull, P. L. Volegov, C. Yeamans, C. Wilde

[a)]**Author to whom correspondence should be addressed:** baker7@llnl.gov

Abstract

In indirect-drive implosions, the final core hot spot energy and pressure and hence neutron yield attainable in 1D increases with increasing laser peak power and hence radiation drive temperature at fixed capsule and hohlraum size. We present simple analytic scalings validated by 1D simulations that quantify the improvement in performance and use this to explain existing data and simulation trends. Extrapolating to the 500 TW NIF peak power limit in a low gas-fill 5.4 mm diameter hohlraum based on existing high adiabat implosion data at 400 TW, 1.3 MJ and 1e16 yield, we find that a 2-3e17 yield (0.5 – 0.7 MJ) is plausible using only 1.8 MJ of laser energy. Based on existing data varying DT fuel thickness and dopant areal density, further improvements

should be possible by increasing DT fuel areal density, and hence confinement time and yield amplification.

I. INTRODUCTION

In indirect drive inertial confinement fusion (ICF) at NIF, a deuterium-tritium (DT) filled capsule[1, 2] is driven by x-rays at peak radiation temperatures Tr of ~300 eV produced by irradiating the inside of a high-Z hohlraum with 192 laser beams entering through two laser entrance holes (LEHs) on either end. The DT hotspot must reach high ion temperatures, T_{ion} >5 keV, and high areal densities, ρr > 0.2–0.3 g/cm^2, to initiate burn, while the total yield depends on the confinement time provided by the total areal density of the DT and remaining ablator, typically designed at 1–2 g/cm^2.

The goal of the National Ignition Facility (NIF) is to increase the liberated fusion energy "yield" in inertial confinement fusion (ICF) experiments well past the ignition threshold and the input laser energy. Most recent efforts have focused on increasing the capsule size to increase the capsule absorbed energy. By using smaller hohlraums with less wall losses, which was the approach pursued in [3, 4], the peak radiation drive temperature T_r can be increased, such that the capsule absorbed energy for smaller capsules can be comparable to larger capsules placed in bigger hohlraums. In addition, the higher T_r leads to higher ablation and hence stagnation pressures for equivalent peak implosion velocity.[5] In this paper we present the results of two sets of DT layered implosions, both of which used 0.844 mm inner radius high density carbon ablators in small hohlraums. The BigFoot experimental campaign[3, 4, 6-15] is shown to follow analytic scaling with laser power and when plotted as a function of capsule absorbed energy to account for differences

in the hohlraum configurations both the BigFoot and HDC[16-21] campaigns are shown to follow the same scaling with yield amplification vs. capsule absorbed energy. Extrapolating the experimental performance of these two campaigns and interpolating the simulations, which match the experiment observables at lower energies, indicate that these implosions would cross into the burning plasma regime at ~1.5 MJ of laser energy. These simulations also predict, assuming low laser plasma backscatter losses and symmetry control can be maintained, that these implosions could reach ignition with a capsule absorbed energy ~175 kJ, ~1.8 MJ of laser energy into a gold-lined hohlraum with 3.45 mm LEHs, with appropriate thicker fuel and ablator. [3, 4] With the typical NIF laser energy of 1.85 MJ and Au-lined DU hohlraums with 3.1 mm LEHs this platform could drive these capsules with up to 200 kJ of capsule absorbed energy and hohlraum temperatures of >335 eV. To help support this, we also present experimental results in which we were able to increase the stagnated cold fuel areal density, by increasing the initial ice thickness. The ability to increase the remaining ablator and cold fuel areal density is critical in increasing confinement time and hence achieving a larger burn-up fraction of the assembled DT fuel and hence higher neutron yield.

In Sec. II, we briefly review the benefits of using smaller capsule and hohlraums using the hohlraum power balance formula. In Section III, we review the experimental parameters from the high-density carbon-based ablator campaigns denoted BigFoot performed in the smallest 5.4 mm-radius hohlraums which used the 192 beam NIF. In Sec. IV, we present simplified capsule rocket model scalings for the purpose of extrapolating from existing data and validate them by comparing to simulation outputs of implosion velocity and mass remaining trends with increasing peak power, laser energy and initial capsule mass. In Sec V we present analytic scalings of hot spot energy, pressure, and ignition metrics in the absence of alpha heating, validated to 1D simulation results

and compare to data and Bigfoot design trends. In Sec VI, we use the analytic formalism to extrapolate to NIF peak power at fixed hohlraum and capsule size, including a discussion of other potential issues such as symmetry control and losses due to laser plasma instabilities. In Sec VII we include yield amplification by alpha heating, first comparing the BigFoot data with many of the campaigns that were carried out on the NIF at higher power and energies in larger hohlraums driving larger capsules, then extrapolating to NIF peak power using a simulated correspondence between the generalized Lawson criterion and yield amplification. In Sec. VIII we discuss the benefits of increasing the DT fuel layer and present the empirical scaling of inferred stagnated fuel areal density as a function of the initial ice thickness. In Sec. IX we summarize the results and extrapolations of the BigFoot 844design with 0.844 mm I.R. HDC capsules and potential further improvements.

II. HOHLRAUM POWER BALANCE

The peak temperature in a hohlraum can be approximated as a power balance between the x-ray power produced in the hohlraum given by the product of peak laser power P_L and fraction converted to x-rays β, and the x-ray power lost to the walls of the hohlraum, the capsule itself and the laser entrance holes (LEH).[6, 22, 23] We note that β also accounts for the fraction of laser peak power lost to backscatter and to the hohlraum He gas-fill used to tamp the high Z hohlraum walls, a few % for the low He gas-fills used currently. The power lost to the walls, capsule and out the LEHs is the x-ray flux inside the hohlraum, σT_r^4, multiplied by their respective surface areas at peak power and the fraction (1 - α) not reradiated, where α is an albedo, yielding:

$$\beta P_L = \sigma T_r^4 [A_w(1-\alpha_w) + 4\pi R_c^2(1-\alpha_c) + 2\pi R_{LEH}^2] \quad (1)$$

where we can define an effective loss area $[A_w(1-\alpha_w)+4\pi R_c^2(1-\alpha_c)+2\pi R_{LEH}^2]$. Typically, $\beta \approx 0.75$ and the ratio of the three terms in the effective loss area comprise 60, 10 and 30% of the total losses[22] with $\alpha_c \approx 0.3$, and $\alpha_w \approx 0.85$ averaged over peak power for the highest practical atomic number Au or U walls available. As T_r increases, by either increasing peak laser power or reducing losses, the albedos also increase such that $T_r^{3.5} \sim P_L$, a scaling used later. The effective loss area of the hohlraum can be minimized by reducing the hohlraum wall's area, increasing the hohlraum wall's albedo, reducing the size of the capsule or reducing the size of the LEH. Most layered implosions use a gold-lined uranium wall to maximize the hohlraum wall's albedo. The minimum LEH size on the NIF is currently limited by the phase plates used by the inner beams. The LEH diameter must be larger than ~1.2x the inner beam footprint in the LEH plane. The two remaining techniques to reduce the losses in the hohlraum are reducing the surface area of the hohlraum wall and the capsule, the strategy employed here.

III. EXPERIMENTAL DESIGN

This paper primarily extrapolates from the NIF campaign, denoted as the BigFoot 844, which used partially W-doped high density carbon (HDC) ablators of inside radius 0.844 mm and thickness between 64 and 68 μm and deuterium-tritium fuel layers between 41 and 45 μm-thick. This BigFoot 844 campaign[3, 4, 6] was conducted in 5.4 mm diameter by 10.13 mm length hohlraums filled with 0.3 mg/cm^3 helium gas and equipped with 3.45 mm LEHs covered with 0.5 μm Lexan windows. The 44.5 and 50° cones were separated in z where they impact the hohlraum wall and each of the outer quads were separated into groups of two beams containing orthogonal polarizations displaced in azimuth to create more uniform illumination of the hohlraum wall. Cone and quad splitting the outers also reduced the intensity on the wall which reduced the gold bubble

expansion velocity where the outers laser beams hit the hohlraum wall to maintain symmetry control and to decrease the growth of laser-plasma instabilities. The BigFoot 844 campaign was designed such that the second shock overtook the first shock in the ablator near the ablator-ice interface with the third overtaking the first two in the gas near the gas-ice interface. As such the ablator was shocked three times and the ice was only shocked twice. This had the effect of stabilizing the fuel-ablator interface, driving a stable (negative) fuel-ablator Atwood number, A, in the acceleration phase of the implosion, where $A = (\rho_f-\rho_a)/(\rho_f+\rho_a)$.[3] Thus, the density of the ablator, ρ_a, is greater than the density of the fuel, ρ_f, throughout acceleration. This was, however, at the expense of a high design fuel adiabat, ~4, due to the larger first combined shock velocity entering the ice layer. The BigFoot design also had the advantage that it required a shorter foot which reduced the ablated mass under inefficient low T_r, low exhaust velocity ~ $\sqrt{T_r}$ conditions. Combined with the use of a 20-30% thinner fuel layer, this leaves more ablator mass remaining for a given peak implosion velocity, as discussed and tabulated further in later sections. The main campaign included four layered DT shots progressively increasing peak power from 310 to 400 TW, laser energy from 1.05 to 1.35 MJ, initial ablator thickness from 64 to 68 μm and DT fuel thickness from 41 to 45 μm.

IV. SIMULATED AND ANALYTIC IMPLOSION SENSITIVITIES

The approach proposed in this article and in [3, 4] is to increase the velocity and performance of a set of BigFoot implosions sharing a fixed capsule design by increasing the laser peak power and energy until a performance cliff is reached due to insufficient ablator mass remaining and too much hydro growth. Just before that point, the capsule and DT ice thickness would be increased to maintain the implosion velocity as laser energy E_L is increased. To anchor this strategy, a series of simulations performed[3, 4] using the two-dimensional radiation hydrodynamics code Lasnex[24, 25]

were presented for the Bigfoot 844 campaign, 0.844 mm radius capsule implosions, starting from the two 320 and 330 TW existing implosions at the time and extending to 500 TW. The two lowest energy simulations were postshots of N161030 and N170109 and the remaining four represent a systematic walkup to the full NIF power. Subsequent experiments at 400 TW, N190721 and N190617, agreed within the error bars, with the simulation and occurred after the BF 950 platform had begun. The simulations used the technique of adding preheat energy, 0.75 MJ/g, to the DT ice layer a few hundred picoseconds before the time of peak implosion velocity (over a period of 100 ps) which increased the design adiabat from α - 4 to $\alpha \sim 5.5$. Adding preheat energy to the DT ice layer allowed the postshot simulations to more accurately reproduce the experimentally measured yield, DSR, T_{ion} and hotspot size and is a surrogate for mix and shock mistiming.

Simulation inputs and outputs are shown in Figure 1 and in Table 1. For all but the 500 TW simulation, the capsule mass and laser peak power pulse length τ is kept fixed as peak power increased. Fig. 1b shows the corresponding remaining mass and coast time decreases as expected as laser power (P_L), energy ($E_L \sim P_L\tau$) and T_r is increased. The coast time is defined as the time between when the laser pulse has dropped to half of its peak power and the time of peak gamma-ray emission, bang time. We note the coast time is kept below 1 ns, a typical hohlraum flux cooling time, as data and simulations show this to be crucial to maintaining high ablation pressure at peak velocity. The simulation performed at 500 TW, 1.9 MJ increased the DT fuel and ablator thickness 20% to prevent burn through and mitigate the effects of hydrodynamic instability growth. This leads to the increase in mass remaining and leveling off of the peak fuel implosion velocity in Fig. 1c.

For quantitatively understanding the simulation trends and extrapolating from newer data, it is instructive to evaluate more broadly the scalings of peak implosion velocity and mass

remaining with capsule mass and peak radiation T_r using a simplified analytic treatment. In the spherical rocket model of an indirect-drive ICF implosion, the peak implosion velocity, v_{imp}, can be expressed in terms of the peak power radiation temperature, T_r, the initial combined mass of the ablator and DT ice, M, and the remaining combined ablator mass and DT ice mass, M_r, as $v_{imp} \sim T_r^{0.5}\ln(M/M_r)$, Over the range of values of M/M_r in these implosions, $7 \leq M/M_r \leq 12$, $\ln(M/M_r)$ approximates as $0.73\sqrt{(M/M_r)}$, hence:[26]

$$v_{imp} \sim T_r^{0.5}\sqrt{(M/M_r)} \quad (2)$$

The rocket equation approximation is valid between $2v_{ex} < v_{imp} < 2.5v_{ex}$, where the exhaust velocity v_{ex} is $\approx 10\sqrt{Tr}$ μm/ns, hence for v_{imp} between approximately 330 and 450 μm/ns.[1] The mass ablation rate, dM/dt, for low Z ablators scales as $T_r^3R^2$ where R is some fixed fraction of the initial radius R_c of the capsule.[27] The ablated capsule mass, $M - M_r \sim M$ since $M_r << M$, then scales over an implosion time τ as:

$$dM/dt \sim M/\tau \sim T_r^3R^2 \quad (3)$$

Case A: Constant Initial Ablator + Fuel Mass M:

Substituting for the implosion time $\tau \sim R/v_{imp}$ in Eq. (3) we arrive at:[28]

$$v_{imp} \sim T_r^3R^3/M \quad (4)$$

As expected, in the hydroscaling limit for which the peak T_r is kept constant and R'= SR, and M' = S^3M the implosion velocity is independent of scale S. Eq. (4) represents the strong increase in v_{imp} as T_r is increased at fixed capsule R and M. Since $T_r^{3.5} \sim P_L$ for fixed hohlraum scale and pulse length, $v_{imp} \sim P_L^{6/7}$. With $v_{imp} \sim T_r^3R^3/M \sim R/\tau_{acc}$ and $P_L \sim T_r^{3.5}$ we can write the acceleration time, τ_{acc}, in terms of the laser power as, $\tau_{acc} \sim P_L^{-6/7}$., where τ_{acc} is the time between the start of

the peak laser power and ~400 ps before the bang time. This is consistent with the peak simulated fuel velocity increasing 13% between P_L = 330 and 420 TW on Fig. 1c and Table 1, when account for peak shell v_{imp} relevant to rocket model increasing faster than fuel velocity being squeezed inward, as ablator mass remaining drops per Fig. 1b.[29]

Case B: Constant Remaining Ablator + Fuel Mass M_r

We now consider the constraint of fixed minimum M_r that is desirable to keep soft x-rays from penetrating the shell and heating the DT fuel directly while still maximizing v_{imp}. Substituting for M from Eq. (2) in Eq. (4):

$$v_{imp} \sim T_r^{4/3} R M_r^{-1/3} \quad (5)$$

Eq. (5) approximates the more detailed derivation in Saillard Eq. (3.39) where $v_{imp} \sim T_r^{1.26} R M_r^{-1/3}$. The lower scaling with T_r can be recovered by including a first order correction in M_r/M. We note the drop in M_r as v_{imp} increases at fixed R and M, consistent with Fig. 1b simulations as increase laser energy up to 1.45 MJ. With $v_{imp} \sim R T_r^{4/3} \sim R/\tau_{acc}$ and $P_L \sim T_r^{3.5}$ we can write the acceleration time, τ_{acc}, in terms of the laser power as, $\tau_{acc} \sim P_L^{-0.38}$., where again τ_{acc} is the time between the start of the peak laser power and ~400 ps before the bang time. Substituting for v_{imp} in Eq (2) using Eq. (5), the scaling of initial mass with peak T_r is given by:

$$M \sim T_r^{5/3} R^2 M_r^{1/3} \quad (6)$$

Eqs. (5) and (6) directly give the scaling of v_{imp} and M with increasing T_r for fixed R and M_r. We note that v_{imp} still increases faster than $v_{ex} \sim T_r^{0.5}$ as allowing for more ablation afforded by more laser energy and by starting with higher capsule mass areal density M/R^2. We can compare this to the rocket model for indirect drive that yields[1] $v_{imp} \sim (R/\Delta R) v_{abl}$. The ablation rate v_{abl} defined as

$(dm/dt)/\rho \approx T_r^{0.9}$, since $dm/dt \sim T_r^3$ and for a given adiabat design, $\rho \sim P^{3/5} \sim T_r^{2.1}$. A more conservative limit,[1, 2] by keeping the in-flight capsule aspect ratio (IFAR = R/dR) fixed, therefore yields $v_{imp} \sim T_r^{0.9}$.

Case C: Constant Peak Implosion Velocity, v_{imp}

For the even more conservative case, approximating that used in simulating the highest laser energy design point on Fig. 1, v_{imp} is held fixed as P_L is raised from 420 to 500 TW(530 Au-U) (E_L from 1.45 to 1.9 MJ) to raise T_r. That limit leads to Eq. (4) simplifying to

$$M \sim T_r^3 R^3 \tag{7}$$

As expected, M increases as a faster power of T_r than in Eq. (6), following the mass ablation rate scaling to zeroth order. Rearranging Eqs. (5) and (2) at fixed v_{imp}, the scaling of mass remaining increases with T_r as

$$M_r \sim T_r^4 R^3 \tag{8}$$

and the fractional mass remaining M_r/M as

$$M_r/M \sim T_r \tag{9}$$

Since $P_L \sim T_r^{3.5}$ from Section II, $M \sim P_L^{6/7}$ and $M_r/M \sim P_L^{2/7}$. Indeed, the design increases M by 20% as the laser power, P_L, is increased by ≈ 26%, from 420 to 530 TW(Au-lined DU). By contrast, the total fractional mass(ice + ablator) remaining M_r/M increases from 10.6% to 11.8%, an increase of ~11%, versus the 7% predicted analytically.

For mitigating hydro-instability feedthrough from the ablation front and maximizing confinement time, the remaining ablator areal density ~ M_r/R_{hs}^2 should be maximized. For a given

design implosion adiabat and v_{imp}, the convergence ratio ~ R/R_{hs} of the implosion is conserved, hence Eq. (7) can be rearranged to give

$$M_r/R_{hs}^2 \sim T_r^4 R \sim (P_L/R_H^2)^{8/7} R \approx P_L(R/R_H)/R_H \quad (10)$$

where R_H is the hohlraum radius. The key point of Eq. (10) is that for the optimum strategy of operating at maximum P_L and R/R_H to optimize coupled energy and still allow for sufficiently uniform x-ray illumination at the capsule, the remaining shell areal density scales as $1/R_H$. This increase in implosion robustness at smaller scale, all else equal, represents an additional advantage to higher T_r increasing the ablation pressure at a given implosion speed[28], lower in-flight-aspect-ratio defined as outer ablator radius divided by the total shell thickness, and stronger ablative stabilization.[22]

V. HOTSPOT METRICS WITHOUT ALPHA HEATING

The simulated product $E_{hs}P_{hs}^2$ for implosions is a convenient metric[30] for likelihood of ignition, where E_{hs} and P_{hs} are the hotspot energy and pressure at minimum volume in the absence of alpha-heating. We now consider the scaling of hot spot energy E_{hs} and pressure P_{hs} with peak power P_L under the constraints of fixed adiabat and capsule and hohlraum scale. We will start by assuming Case C, that the implosion time ~ R/v_{imp} and hence the peak implosion velocity v_{imp} is approximately held fixed as P_L and hence T_r is increased by appropriately thickening up the capsule and DT fuel. That will ensure nearly fixed hohlraum to capsule coupling efficiency. Moreover, simulations of ignition-relevant indirect-drive designs show that the coupling efficiency to the capsule kinetic energy at peak v_{imp}, known as "rocket efficiency", is a weak function of any mass remaining[2] and v_{imp} variability. Finally, the coupling efficiency η_{hs} of imploding kinetic energy

$1/2M_r v_{imp}^2$ to E_{hs} in indirect-drive, for fixed v_{imp} and ratio of DT fuel mass M_{DT} to total remaining mass M_r, is ≈ constant, at ≈ 25% near ignition of HDC-based designs. [30] Hence, simulations under this constraint of fixed hohlraum and capsule scale and v_{imp}, and increasing M_{DT} in proportion to M_r as approximately designed between 420 and 530 (Au-lined DU) TW per Fig. 1 and Table 1, predict E_{hs} approximately scaling with P_L. We can understand this by applying the simplified rocket model developed in the previous section. Substituting for v_{imp} from Eq. (2):

$$E_{hs} \sim \eta M_r v_{imp}^2 \sim T_r M \tag{11}$$

and further substituting for M using Eq. (7):

$$E_{hs} \sim T_r^4 R^3 \sim P_L^{8/7} \tag{12}$$

We now wish to evaluate P_{hs}. We start with assuming adiabatic hot spot compression (PV^γ conserved) between the time of peak velocity (subscript pv) and stagnation (subscript hs) ([9, 31]) such that assuming ideal gas $\gamma = 5/3$:

$$P_{hs} R_{hs}^5 \sim P_{pv} R_{pv}^5 \tag{13}$$

Eq. (13) has implicitly assumed the pdV work dominates over the sum of the alpha heating gains and radiative losses.[32] That sum is 0 at $T_{ion} \sim 4.3$ keV, typical of the lowest yield implosions considered here that are used to normalize the scaling. 1D simulations[30] show that R_{pv} is constant to the 1% level as peak T_r is varied for a given low coast implosion design, so we can simplify to:

$$P_{hs} R_{hs}^5 \sim P_{pv} \sim T_r^{3.5} \sim P_L \tag{14}$$

where we have equated pressure at peak v_{imp} as scaling with peak ablation pressure ~ $T_r^{3.5}$, which is valid for short coast times, <0.5 ns.[33] Substituting for R_{hs} from Eq. (14) into the definition of $P_{hs} \sim E_{hs}/R_{hs}^3$ and for E_{hs} using Eq. (12):

$$P_{hs} \sim T_r^{19/4} \sim P_L^{9.5/7} \tag{15}$$

Hence the ignition metric $E_{hs}P_{hs}^2$ scales as $P_L^{27/7}$ for fixed v_{imp}(case C), increasing by a significant 2.0x between the P_L = 420 and 500 TW designs.

Figure 2a and 2b show the measured(green circles) and simulated(black circles) hotspot pressures(2a) and energies(2b) for the BigFoot 844 campaign. These were calculated assuming a uniform hotspot model and include alpha heating.[34] To understand the contribution to alpha heating a dataset of implosions with a wide range of final adiabats, with and without alpha heating, was used to determine the pressure($P_{hs\text{-}amp}$) and energy($E_{hs\text{-}amp}$) amplification factor as a function of yield amplification.[35] For this database, the pressures and energies were again calculated using the uniform hotspot model and the fits to the pressure and energy amplifications are listed in Fig. 2a and 2b, respectively. The with alpha heating curves in the figures are then the without-alpha analytic results multiplied by the amplification factors. The circle diameters of the with-alpha heating numbers are proportional to the square root of the yield amplification.

For Case A, assuming fixed M, we start with Eq. (2) including η_{hs}:

$$E_{hs} \sim \eta_{hs} M_r v_{imp}^2 \sim \eta_{hs} T_r M \sim P_L^{11/7} \tag{16}$$

where the last expression is derived from 1D simulations[30] showing that η_{hs} scales as $P_L^{9/7}$ for fixed M. We can understand this by recognizing that η_{hs} is the ratio[30] of hotspot volume R_{hs}^3 to total shell + hot spot volume $(R_{hs} + \Delta R)^3$ assuming an isobaric system. The shell thickness ΔR decreases

as increase P_L, both due to increased P_{pv} and hence stagnated shell density and due to a larger fraction of the remaining mass being the cooler, hence denser DT fuel. Hence using Eqs. (14) and (16), $P_{hs} \sim P_L^{17/7}$ and the ignition metric $E_{hs}P_{hs}^2$ scales as $P_L^{45/7}$ for fixed M. We also note that $R_{hs} \sim (E_{hs}/P_{hs})^{1/3} \sim P_L^{-2/7} \sim 1/T_r$, shrinking slightly as laser power and ablation pressure increases in the absence of alpha heating, consistent with those same simulations. Again, the with alpha heating curves in figures 2a and 2b are the without-alpha analytic results multiplied by the amplification factors. Thus, in 1D, E_{hs}, P_{hs} and the ignition metric scale faster with P_L as we transition from the most conservative Case C, fixed v_{imp}, to the least conservative Case A, fixed M. Based on the good match between data, simulated and analytic power laws, we estimate that the power law exponents in the analytic model are good to 10-20% over the ranges displayed.

Case B, assuming fixed M_r, applies closest to the transition between the 325 and 500 TW BigFoot shots. Substituting for v_{imp} from Eq. (5) and assuming an intermediate scaling $\eta_{hs} \sim P_L^{0.5}$:

$$E_{hs} \sim \eta_{hs} M_r v_{imp}^2 \sim \eta_{hs} T_r^{8/3} R^2 M_r^{1/3} \sim \eta_{hs} P_L^{16/21} \sim P_L^{53/42} \quad (17)$$

and using Eqs. (14), (17) and (5):

$$P_{hs} \sim P_L^{139/84} \sim T_r^{139/24} \sim v_{imp}^{139/32} \quad (18)$$

As a check, we note the final expression matches detailed derivation for Case B) in [36] Eq. (4.45) $P_{hs} \sim v_{imp}^{14/3}$. The ignition metric $E_{hs}P_{hs}^2$ then scales as $P_L^{32/7}$ for fixed M_r.

We can compare campaigns using different hohlraum configurations by plotting capsule absorbed energy.. The capsule absorbed energy can be approximated as $E_{cap} = 57.(R_c)^2 E_L L_m / A_L$, where R_c is the capsule outer radius in mm, L_m is the hohlraum wall material multiplier (1 for Au, 1.06 for U or 1.065 for Au-lined U), A_L is the hohlraum loss area in cm^2 calculated from Eq. (1)

(assuming a wall albedo of 0.86) and E_L is laser energy delivered to the hohlraum (reduced by the inferred level of backscatter). This simple expression for the capsule absorbed energy agrees fairly well with a sampling of the capsule absorbed energy derived from integrated hohlraum and capsule-only simulations. We obtain similar results using the definition $E_{cap} = 100(R_i)^3 P_L L_m/(A_L v_{imp})$, where E_L is replaced by $P_L R_i/v_{imp}$. In this case P_L is the peak laser power delivered to the hohlraum (reduced by the inferred level of backscatter), R_i is the capsule inner radius in mm and v_{imp} is the peak implosion velocity. In Fig. 2c we have plotted the capsule absorbed energy as a function of laser power for the BigFoot 844 implosion simulations. In Fig. 2d we use the results from Fig. 2c to show the pressure vs. capsule absorbed energy where we have now included the HDC 844campaign which also used 0.844 mm inner radius capsules. By plotting the pressure in terms of capsule absorbed energy we can see that the different campaigns have a similar pressure vs. capsule absorbed energy curve, even though the experiments were carried out in different size hohlraums with different laser energies and powers. We note that the capsule absorbed energies (E_{cap}) for the BigFoot and HDC 844 implosions are all less than 130 kJ at the modest laser energies and wall materials the experiments were carried out in but that they could be pushed to 200 kJ,

VI. PEAK POWER EXTRAPOLATION

We now have all the formulas required for scaling hot spot performance from the existing shot N190721 at 400 TW(Au hohlraum) to current NIF peak power capability of 500 TW(effectively 530 TW in a Au-lined U hohlraum). The foot pulse length will be assumed to scale with ablator + DT fuel thickness hence approximately as M for fixed R. The peak power

duration τ should scale as $1/v_{imp}$ for assuring constant coast time, hence E_L scales $\approx$ as P_L/v_{imp} by ignoring any foot length and hence foot energy changes at 10x lower power mandated by capsule thickness changes. Table 3 gives the various input and output values for extrapolating from N190721 400 TW to 500 TW peak power assuming the 3 cases of constant M, constant M_r and constant v_{imp}. In addition, we have added a case for constant M_r replacing the Au with Au-lined DU hohlraum that is predicted based on prior data[37-39] to increase wall albedo such that the effective peak power is 6% larger per Eq. (1). Also listed on the last column Table 3 is the ignition metric $E_{hs}P_{hs}^2$ normalized to N190721. The threat of x-rays burning through the ablator and leading to unstable Atwood number at ablator/fuel interface or penetration of ablation front hydrodynamic instability growth suggests keeping $M_r/M > 9\%$ such that the remaining ablator mass is no less than the 4-4.5%, equivalent to the DT fuel mass. Combined with maximizing the ignition metric, we choose to concentrate on further exploring the fixed M_r case ultimately using a Au-lined U hohlraum for higher coupling efficiency. This suggests the ignition metric can be increased 3.6x.

Figure 3 compares the pulse shape used for N190721 to the pulse shape required for maintaining fixed M_r at the maximum NIF peak power of 500 TW per the analytic scalings presented earlier. The pulse foot is 12% longer to provide the same shock timing for the 12% higher mass capsule while the peak power duration $\tau \sim 1/v_{imp}$ is 9% shorter. A rocket model of the two pulse shapes/designs predicts that their percentage mass remaining are within 10 percent of one another, 7.3% vs. 7.8%.

It is worthwhile revisiting at this point increasing the scale since Table 3 shows the full NIF 1.9 MJ energy not being used given the short (< 3 ns) implosion times. Per Eq. (1), in the BigFoot 844 platform, with an 0.844 mm I.R. capsule in a 5.4 x 10.13 mm gold hohlraum with

3.45 mm LEHs, the surface wall area of the hohlraum is 1.86 cm^2 with an effective loss area of 0.51 cm^2. In comparison the BigFoot 950 platform, which used a 0.95 mm I.R. capsule in a 6.0 x 11.3 mm gold hohlraum with 3.9 mm LEHs. the wall area is 2.28 cm^2 has an effective loss area of 0.64 cm^2. Assuming that both hohlraums are driven by the same 500 TW peak power pulse then the peak power radiation flux inside the hohlraum, T_r^4, will be 0.64/0.51 = 1.25x higher in the smaller hohlraum. Per Eq. (12), the hot spot energy E_{hs} for the smaller hohlraum and capsule is $1.25(0.844/0.95)^3 = 0.9$x, smaller. However, since the smaller hohlraum $P_{hs} \sim T_r^{19/4} = 1.3$x per Eq. (15) more by virtue of being hotter, its ignition metric $\sim E_{hs}P_{hs}^2$ is significantly higher, 1.5x.

We now consider the drive symmetry control and laser plasma instability challenges as increase peak laser power. Going to full NIF power in the 5.4 by 10.13 mm hohlraums with 0.844 mm inner radius HDC capsules is expected to have a small effect on implosion symmetry. Specifically, we expect based on empirical models[40, 41] of inner beam propagation impairment due to ballistic capsule ablation and outer beam spot wall blow-off that the longer foot would only produce a shift in the core x-ray emission P2 of -10.5 μm. N190721 had a round neutron hotspot with an inner beam peak power cone fraction of 31%. Going to 500 TW on the NIF, we can increase the inner cone fraction to a maximum of 33% which reduces the asymmetry in P2 to -4.5 um which could be zeroed out with < 0.5 Å of wavelength differential between the inner and outer cones promoting cross beam energy transfer (CBET). Time-dependent P2 symmetry swings can be mitigated using techniques such as staggering beam cones in time to counter wall motion[42].

Laser plasma instability losses could potentially limit peak power absorbed, especially as the plasma filling density increases in the hohlraum given 15% more incident laser energy and capsule ablation. However, there is very little measured LPI losses currently at 1.35 MJ, < 1%, and SBS on the 50° cone can be reduced by application of a wavelength separation between 50°

and 45° cones to promote CBET from the 50° to the 45° cone if it becomes a concern at higher power.[43] That leaves the potential of increased SRS losses on the inner beams due to both higher peak power and density, though to date no 0.3 mg/cm^3 fill HDC campaign has measured any significant level of SRS. One could reduce the hohlraum gas-fill slightly to counter the increased capsule ablation.

VII. YIELD AMPLIFICATION

In an inertially-confined fusion (ICF) implosion with a DT fuel layer, each fusion reaction of deuterium and tritium ions generates a 14.1 MeV neutron and 3.5 MeV alpha-particle.[7] The stopping ρR for an alpha-particle, however, is only ~0.1-0.2 g/cm^2 at an ion temperature, T_{ion}, of 4 keV, which is characteristic of the hot-spot ρR and T_{ion} conditions achieved in many ICF implosions on the NIF. Each of the alpha-particles stopped within the hot-spot deposit their 3.5 MeV of energy, thereby increasing the hotspot ion temperature, T_{ion}, and subsequently the reactivity-rate. The alpha-particles stopped in the cold fuel heat and ablate the fuel into the hot-spot, increasing the hotspot mass (M_{hs}) and the hot-spot ρR which enables more of the subsequent alpha-particles to be stopped within the hot-spot. When the fusion reactions heat the hotspot faster than loss mechanisms cool it, external energy is no longer required to heat the fuel and fusion ignition occurs. Another very important measure of performance in layered implosions is therefore the level of alpha heating present in the implosion.

The yield amplification, Y_{amp}, as a function of laser energy for the different NIF campaigns are shown in Fig. 4a, where Y_{amp} is the ratio of the measured yield in an experiment to the yield if there was no alpha heating or $Y_{amp} = Y_{DT}/Y_{DT\alpha\text{-off}}$. The yield amplification was calculated based on fitting simulations of BigFoot implosions using the formulas[7]

$$\text{ITFXmod} \sim (19.7*\text{DSR})^2*(0.24*(4f_Df_T)*Y_{13\text{-}15}/M_{fuel}) \quad \text{and} \tag{19}$$

$$Y_{amp\text{-}ITFXmod} \sim \exp(\text{ITFXmod}^{0.446}), \tag{20}$$

where DSR is the down scattered ratio (a ratio of the neutron yield in the fuel-scattered neutron kinetic energy range from 10 - 12 MeV to the 13 - 15 MeV unscattered yield), f_D is the deuterium fraction in the hotspot, f_T is the tritium fraction in the hotspot, $Y_{13\text{-}15}$ is the primary neutron yield/10^{16} and M_{fuel} is the initial mass of the ice layer in mg.

The diameter of the points in Fig. 4a represents symbolically the initial surface area of the capsule, ranging from an inner capsule radius of 0.833 to 1.1 mm. The Bigfoot shots are represented as green circles where the shots performed with 0.844 mm capsules in the 5.4 x 10.13 mm hohlraums are all below 1.4 MJ. The red circles are HDC shots below 1.2 MJ using 3-shocks all merging near the DT fuel/gas interface of 0.844 mm capsules in 5.75 x 10.13 mm hohlraums. If we account for differing hohlraum efficiency between gold (e.g. used for BigFoot), uranium (e.g. used for HDC) and gold-lined uranium-based campaigns then we can plot the yield amplification as a function of capsule absorbed energy for the various campaigns in Figure 4b. We see that the capsule absorbed energies (E_{cap}) for the BigFoot and HDC 844 implosions were less than 130 kJ at the laser energies and wall materials the experiments were carried out in. Hence the 844 campaigns have been significantly more efficient at achieving a given yield amplification value approaching the burning plasma regime. In addition from Fig. 4a we can see that the BigFoot 844 implosion at 1.3 MJ and 400 TW, N190721, carried out in a gold hohlraum achieved a higher yield amplification than the majority of the campaigns on the NIF conducted at full energy and power with higher albedo hohlraum walls(including the HyE 1100[44, 45], HyB[46, 47], LF[38, 48], HF[49-51], HF low fill[39, 52] and ASHF[53-55] campaigns). Only the BigFoot 950, HDC 910, Iraum 1000[56] and HyE 1050[57-59] campaigns achieved higher performance than N190721, but only achieved this at

the full NIF energy and power. The question then becomes, what does it take for an 844 design to reach the burning plasma and ignition regime?

To assist in answering this, Fig. 5 highlights the four BigFoot 844 implosions, as smaller green circles, the BigFoot simulations[3, 4], as black circles, the HDC 844 implosions, as red circles, as well as the neutron-imaged hot spot cores of the BigFoot experimental data. Also included are two Iraum, brown circles, and HyE 1050, gray circles, shots which recently crossed the burning plasma and the one HyE 1050 shot that crossed the ignition threshold.[59] As shown in Fig. 5c, the simulated yield amplifications have ± 20% error bars. This is consistent with measurements of Y_{amp} using DT/THD pairs at lower yield amplification levels.[7] The hotspot for N190617 at 1.35 MJ was very prolate, $P_2/P_0 \sim 56\%$, to which we attribute its drop in yield and yield amplification relative to a rounder hotspot. Interpolating the simulations, they predict that this BigFoot 844 platform would enter the burning plasma regime ($Y_{amp} > 3.5$) at a laser energy of 1.5 MJ (430 TW) and reach ignition with a capsule absorbed energy ~175 kJ, using ~1.8 MJ of laser energy into a gold-lined hohlraum equipped with 3.45 mm LEHs, and appropriately thicker fuel and ablator. [3, 4, 12] With the typical NIF laser energy of 1.85 MJ and Au-lined DU hohlraums with 3.1 mm LEHs this platform could drive these capsules with up to 200 kJ of capsule absorbed energy for these 844 μm inner radius capsules.

The generalized Lawson criterion, GLC, has been used in both direct and indirect drive to determine the proximity of an implosion to ignition. Conveniently, the GLC, excluding alpha heating, scales as the square root of the Ignition metric $E_{hs}P_{hs}^2$ derived previously[30, 60],

$$GLC(P_{hs}, E_{hs}) = P_{hs}(Gbar/280)\left(E_{hs}(kJ/4)\right)^{0.5} \quad (21)$$

So, it follows that the 500 TW design using a Au-lined U hohlraum on the lowest row of Table 3 promises a $\sqrt{3.6}$ = 1.9x higher GLC in 1D than shot N190721. Furthermore, published 1D simulations provide the relationship between Y_{amp} and GLC, in this case for an idealized BigFoot design as vary peak power, as shown by the black points and fitted curve on Fig. 6. So, scaling from the measured Y_{amp} = 2.6 of N190721 on that curve, the green point, that happens to be at GLC ≈ 0.62, we predict a Y_{amp} of ≈ 18 for a 500 TW extrapolation that corresponds to a GLC that is $\sqrt{3.6}$ higher, at 1.18. This is consistent with the 500 TW simulation Y_{amp} of 17 on Fig. 4. One can also rewrite the neutron yield in terms of the yield amplification and peak power as follows,

$$Y \sim Y_{amp} n_i^2 T_i^{3.5} R_{hs}^3 \tau_{bw} \sim Y_{amp} T_r^{11} \sim Y_{amp} P_L^{3.2} \approx Y_{amp} P_{hs}^2 \quad (22)$$

where the DT fusion reaction rate ~ $T_i^{3.5}$, $R_{hs} \sim 1/T_r^{0.45}$ per Eqs. (14) and (18), and for given design and per 1D simulations $T_i \sim T_r^{3.3}$ and $\tau_{bw} \sim 1/T_r^{3.5}$. Hence given the N190721 yield of 1.1×10^{16}, a 500 TW (530 TW effective given Au-lined DU) design yield extrapolates using Table 3 and Eq. (22) to 1.1×10^{16} x 18/2.6 x $(530/400)^{3.2} = 1.9 \times 10^{17}$ or 0.5 MJ, all else equal.

The analytic scaling for pressure and energy, without alpha heating, along with the pressure and energy amplification scalings can then be compared to the GLC(with alpha heating) = $P_{hs}(E_{hs})^{0.5}$ from the BigFoot simulations. In particular, the P_{hs}, $P_{hs\text{-}amp}$, E_{hs}, and $E_{hs\text{-}amp}$ scaling with laser power for case A of $P_L^{17/7}$, $P_L^{0.8}$, $P_L^{11/7}$, and $P_L^{1.5}$, respectively, leads to a case A GLC(with alpha heating) ~ $P_L^{4.8}$. This is in excellent agreement with the fit of the simulated BigFoot results shown in Fig. 5a of GLC ~ P_L^5. Likewise, the P_{hs}, $P_{hs\text{-}amp}$, E_{hs}, and $E_{hs\text{-}amp}$ scaling with laser power for case C of $P_L^{9.5/7}$, $P_L^{1.5}$, $P_L^{8/7}$, and $P_L^{4.7}$, respectively, leads to a case C GLC(with alpha heating) ~ $P_L^{5.8}$. This is in reasonable agreement with the fit of the simulated BigFoot results shown in Fig. 5a of GLC ~ $P_L^{5.1}$. Again, using the relationship between P_L and E_{cap} from Fig. 2c we arrive at the

analytic scalings for GLC as a function of E_{cap} for case A of GLC ~ $E_{cap}^{4.8}$ and for case C which is also GLC ~ $E_{cap}^{4.8}$. This is then in reasonable agreement with the scalings in Fig. 5b for case A of GLC ~ $E_{cap}^{4.8}$ and for case C which is also GLC ~ $E_{cap}^{3.9}$. Figure 5c then shows the yield amplifications as a function of capsule absorbed energy for the BigFoot experimental data(green circles) and simulations(black circles), the HDC data(red circles) and the best performing Iraum(brown circles) and HyE(grey circles) implosions. The yield amplification scalings for the BigFoot simulations in case A, Y_{amp} ~ 1 +1.8x$10^{-12}E_{cap}^{5.7}$, and case C, Y_{amp} ~ 1 +1.6x$10^{-13}E_{cap}^{6.2}$, show similar power scalings with capsule absorbed energy. Again, by plotting the yield amplification as a function of capsule absorbed energy, we can see that both the BigFoot and HDC implosions using 844 μm I.R. HDC capsules have similar performance of yield amplification vs. capsule absorbed energy and are more efficient(lower E_{cap}) at reaching a given yield amplification level than the larger best performing IRaum(1000 μm I.R.) and HyE(1050 μm I.R.) campaigns. The ignition threshold, GLC = 1, is plotted for the BigFoot simulations suggesting that the ignition threshold could be reached with a capsule absorbed energy ~175 kJ, ~1.8 MJ of laser energy into a gold-lined hohlraum with 3.45 mm LEHs. One could further improve the GLC and hence Y_{amp} and yield of the 500 TW BF 844 design by reducing the LEH size to 3.1 mm to improve the coupling by 6%, P_{hs} by 10%, GLC by ≈ 10%, Y_{amp} to its maximum simulated value of 20, shown in Fig. 6, for this design adiabat and yield to 0.7 MJ. However, more impactful options potentially exist: lengthening the laser pulse to optimize the shock timing for reduced adiabat (employed by the HDC 844 campaign) or better quality more highly doped capsules to reduce mix and reduce the adiabat to increase the compression, confinement time and hence Y_{amp}(>30) and increasing the DT fuel layer thickness to further increase the fuel areal density and the achievable burn-up fraction and maximum Y_{amp} as discussed next.

VIII. STAGNATED FUEL AREAL DENSITY

In this section we compare the DSRs from many of the campaigns on the NIF, sorted by the initial ice thickness and further sorted by dopant level and coast time in Fig. 7a and 7b. Only shots with $Y_{amp} < 3$ are plotted as the DSR is expected to drop slowly with increasing yield amplification (by $\sim$4% at $Y_{amp} = 3$) as alpha-heating leads to an explosion phase before peak burn. The residual DSR variations within a given campaign or between campaigns can be attributed to variations in delivered shock strength and timing affecting adiabat[61, 62], level of mode 1 and mode 2 drive asymmetries[63, 64], dopant areal density (as depicted by size of circles in Fig. 7a) affecting Atwood # at interface and hence level of fuel/ablator mix, coast time[65] (depicted by size of circles in Fig. 7b) , level of multi-keV x-ray preheat spectrum set by peak laser intensity, hohlraum wall material[66] and hohlraum temperature, hohlraum geometry[56, 67] and potentially level of > 170 keV hot electrons preheating the inner ablator layer and the fuel[68].

A) Thicker DT Ice

In [3, 4] it was pointed out that the DSR between experiments carried out on two different platforms with two separate ablator materials had measured maximum experimental DSRs that were proportional to the initial ice thickness in the two separate campaigns. We have extended that in Fig. 7a and 7b to include the DSR achieved on many platforms conducted on the NIF, including both HDC and CH implosions. This figure shows that the maximum DSR increases with increasing initial DT fuel thickness. As such, thickening the DT fuel can be an important way to increase the burn-up fraction in layered implosions and lead to higher performance.[3, 4] The fractional burn-up of the fuel, ϕ, in a robustly igniting ICF plasma can be represented[2] by $\phi = \rho r/(\rho r + \rho r_B(T_{ion}))$ where

ρr is the total areal density, ρr, of the imploded mass of fuel and remaining ablator, and $\rho r_B(T_{burn})$ is a decreasing function of T_{ion}, asymptoting to 6 g/cm^2.

To directly measure the effect of a thicker ice layer on DSR, a comparison experiment, N180317, was carried out in the HDC platform where the ice thickness was increased by 11.6 μm, 66.6 μm vs. 55 μm, over 4 other experiments repeating N170827. The pulse shape on N170827 and repeats was lengthened on N180317 to keep the shock timing the same through the thicker ice layer and to maintain a similar velocity between the experiments. The DSR measured in the two sets of experiments increased from 3.13 ± 0.2 to 3.68 ± 0.2, increasing by 18% as the DT ice layer was increased by 21%. The velocity of the two experiments was estimated to be the same within error bars, 408 ± 10 km/sec on N170827 to 404 ±10 km/sec on N180317. The bang time increased from 8.18 ns to 8.66 ns, consistent with the expected 0.4 ns increase in the laser pulse lengths, 7.8 vs. 8.2 ns, needed to maintain the shock symmetry through the thicker ice layer.

In the set of four layered implosions that were performed in the BigFoot 844 platform in the 5.4 x 10.13 mm hohlraum, the ablator thickness and ice thickness were increased on the latter two shots relative to the initial two while keeping the hohlraum and the capsule inner radius fixed as detailed in Table 2. For these two latter shots, the ice thickness was increased by 9.3%, the ablator thickness by 5.9% and the laser energy increased from 1.1 MJ to 1.33 MJ relative to the previous two implosions in this platform. The average DSR for the two shots with the thicker ice/ablator increased by 11.6% per Table 2. However, the higher DSR was partially due to a 5% higher velocity, a 3% effect assuming DSR ~ $v_{imp}^{0.6}$. In addition, across all the BigFoot implosions, 844 and 950 scales, there were roughly three ice layer thicknesses employed: 40, 45 and 50 μm. As seen in Fig. 7a and 7b at each of these ice thicknesses the peak DSR falls close to the dashed line, DSR in % = 0.069 x ice thickness in μm.

Subsequent to these experiments, a variety of thicker DT ice layers spanning 57 to 76 μm was used in the HyE1100 campaign.[44, 45] The nanocrystalline HDC ablators used in these experiments had numerous internal defects, voids, and surface pits whereas the internal voids at least were believed to be largely absent from the experiments described above (except for the HyB capsules) which used microcrystalline capsules. These poorer quality nanocrystalline capsules likely contributed to the lower DSR/(μm of ice) seen in the HyB and HyE1100 campaigns by mixing more ablator material into the ice layer. Unlike BigFoot and HDC campaigns, the HyE1100 DSR did not vary with ice layer thickness for a given coast time , perhaps because of the poorer capsule quality The yield of the implosions, however, increased by up to a factor of two with the thicker ice layer. Recently nanocrystalline capsules with high dopant levels have been developed which are of much higher quality than the previous nanocrystalline or microcrystalline capsules and should lead to reduced mix and increased DSRs relative to the capsules used in earlier campaigns.

B) Coast Time

Fig. 7b shows that the DSRs within a given design increases as coast time decreases, as noted previously for subsets of the data shown here. The clearest examples are within the CH LF, CH HF, HDC, and HyB series where coast times varied significantly (from as low as 0.5 to as high as 2 ns). The optimum use of a given laser energy and power would leave the laser drive on until to just before deceleration time, so typically a coast time of 0.5 ns before bangtime, scaling with capsule size / peak velocity, as assumed in Sections IV – VII Long coast times, >1.2 ns, were present in the HyE 1100 and HyB campaigns because using larger capsules, hohlraums and LEHs,

leading to lower DSR values.. So use of a smaller hotter hohlraum and capsule should also relax the requirements on laser energy required to maintain short coast times.

C) Design Adiabat

The no-alpha heating DSR[26] is also expected to depend on the adiabat and velocity of the implosion according to DSR ~ $\alpha^{-0.8} v_{imp}^{0.6}$. Indeed, the highest DSR/(thickness of ice) is seen for the CH LowFoot (LF) shots (teal points) which have a significantly lower design adiabat <1.6 than the other campaigns and hence higher convergence. A case where two different campaigns can be compared to look at the effect of adiabat on compression is the adiabat-shaped high foot and the high foot campaigns. In the adiabat-shaped high foot campaign (red points) the trough was lower relative to the high foot campaign (blue points), which allowed the first shock to decay as it travelled through the ablator and enter the DT ice layer at a lower velocity than the high foot campaign and hence led to a lower adiabat and higher compression.[53, 55] As shown in Fig. 7a and 7b, the peak DSR in the adiabat shaping campaign was ~15% higher than in the high foot campaign with equivalent capsule dopant, similar implosion velocity and coast time..

While going to lower adiabat has led to higher compression and DSR in plastic implosions this has not been as apparent in the HDC ablator implosions. Given the DSR dependence on design adiabat, it would be expected that the BigFoot campaign would have a lower DSR/(thickness of ice) than most of the campaigns on the NIF due to its higher design adiabat, α=4. However, what is seen in Fig. 7 is a linear relationship for the maximum DSR vs. ice layer thickness across many of the platforms including the BigFoot (green points), Adiabat-Shaped High Foot (red points), Iraum (black points), Low-Fill High Foot (light gray points) and the HyB (brown points)

implosions consistent with these platforms having a similar fuel convergence ratio despite their different design adiabats.[26] The Iraum campaign used both a higher picket power/energy, ~20%, and lower trough, ~27%, than the HyE campaigns[69] leading to a decaying radiation temperature in the hohlraum[69] which could have contributed to the higher DSR performance in that campaign.[70] However, the Iraum also had a higher W areal density content as discussed in the next section.

D) Dopant Level

The level of dopant in the ablators may also play a role in the maximum achievable DSR in DT implosions.[20, 51, 71] The dopant layer shields the undoped ablator layer in contact with the DT fuel layer from higher energy x rays, >1.8 keV, which allows it to be compressed to a higher density and makes the fuel-ablator interface more stable, though the higher dopant level increases ablation front instability which if bad enough can alsoreduce the average DSR. The diameter of the circles in Fig. 7a are a function of the dopant areal densities. The diameter of the circles in the HDC campaigns are normalized to the areal density of W dopant where the smallest circle represents 0 μm% W dopant in the HDC capsules. The diameter of the circles in the CH campaigns are normalized to the atom percent of Si dopant where most of the circles represent 1xSi dopant in the CH capsules, defines as 2% by atomic fraction Si in the most doped layer. The undoped HDC experiments had very low DSR values, as seen by the small yellow and green circles towards the bottom left of Fig. 7a, although as seen in Fig. 7b these alsocorresponded to long coast times, up to 2 ns, which reduces the DSR. In addition, some of the more recent campaigns utilizing HDC ablators used higher tungsten dopant areal densities than the HDC and BigFoot campaigns. The Iraum campaign is the only HDC platform to exceed the DSR/(μm of ice) of the BigFoot campaign and it did so with longer coast times as seen in Fig. 7b. Fig. 7a shows that the Iraum capsules had much higher W dopant areal density, ρR, than the HyE 1050, BigFoot and HDC capsules by >30%

and a slightly higher mass for their scale (thickness).[6] Higher dopant areal densities would have likely allowed these earlier campaigns to go to a higher value of DSR/(μm of ice).

Putting the full NIF energy into a smaller hohlraum is expected to increase the radiation temperature relative to current hohlraums. As stated, the radiation temperature could rise from 315 eV in the larger hohlraums to 335 eV. Currently the m-band fraction of the hohlraum drive, x-ray energies >1.8 keV, is about 20%. The Planckian component of this m-band fraction at 315 eV is ~16.5%. At 335 eV we would expect a Planckian component of ~20%. Thus, we would expect the m-band fraction to increase from ~20% to ~24% at the higher Tr which would require a small increase in the dopant areal density to account for the 20% increase in the number of x-rays above 1.8 keV, as well as their higher fluence on the capsule due to the closer proximity of the outer beams to the capsule with the smaller size of the hohlraum.

E) Ablation Front Stability

Adiabat shaping was also used to increase the ablation front stability to achieve increased performance in the adiabat-shaped low foot campaign by increasing the picket energy.[53] The first shock had a higher initial pressure as it traveled through the ablator, helping to stabilize the ablation front, but decayed as it traveled through the ablator such that it entered the ice layer at a similar pressureas the constant supported first shock driven in the low foot campaign such that the design adiabats were similar.[53, 55] The adiabat-shaped low foot campaign (orange point) as seen in Fig. 7a and 7b, achieved a similar DSR, ~5% higher, at the 1xSi dopant level as the best performing(DSR wise) low foot layered implosion (light blue points), though the adiabat-shaped low foot implosion had a shorter coast time, ~150 ps, than that low foot implosion. The yield and yield amplification for the adiabat-shaped low foot implosion were higher than all of the low foot layered

implosions.[54, 55] The reduction in the ablation front growth in the adiabat-shaped low foot implosion likely reduced the feed through of localized engineering perturbations such as the tent scar and fill tube.

F) Hot Electrons

Reduction of parametric instabilities, in particular stimulated Raman scattering and two plasmon decay which create hot electrons in the damping of the Langmuir waves could also be important in achieving higher DSRs . These hot electrons can deposit their energy into the DT fuel making it more difficult to compress and lowering the achievable DSR for the implosion. This is one of the differences between the 1,6 mg/cc ^{4}He hohlraum fill high foot CH campaign (blue points) and the 0.6 mg/cc hohlraum-fill high foot CH campaign (gray points), though the first low-fill high foot CH also had a lower first shock speed. The high and low gas-fill campaigns experienced SRS backscatter of 10-15% and 2-3%, respectively. and the former also showed superhot electrons likely from two-plasmon decay [68] As seen in in Figure 7 the best performing low-fill high foot implosion had 15% higher DSR/(μms of ice) than the best performing high foot implosionfor similar design adiabat and implosion velocity.

IX. SUMMARY

Most efforts to improve performance of layered implosions to date have focused on increasing the capsule size to increase the surface area and the capsule absorbed energy. In this article we expound upon our approach in [3, 4] where we reduce the losses using a smaller hohlraum to increase the radiation drive power. The higher drive enables a comparable capsule absorbed energy with smaller surface area capsules. By increasing the laser peak power, the higher T_r drive on the smaller capsule should enable both a higher hot spot energy and pressure than present for the larger capsules in larger hohlraums driven with more energy. Specifically, from analytic

scaling of the rocket model of implosions validated by simulations, the generalized Lawson criterion ~ $E_{hs}^{0.5}P_{hs}$ increases as ≈ $P_L^{2.3}$, hence by almost 2x going from existing 400 TW implosions in a Au hohlraum to the NIF 500 TW peak power limit in a higher albedo Au-lined U hohlraum. This in turn should allow prior 844 implosions that reached a Y_{amp} of 2.5 to reach burning plasma and near ignition conditions (0.5 – 0.7 MJ), even with as little as 1.5 to 1.7 MJ of laser energy.

For further improvements, the ability to increase the fuel areal density and hence confinement time at stagnation is predicted to be critical in achieving a larger burn-up fraction of the assembled DT fuel and subsequently in achieving higher yields and performance. In this article we also showed that the maximum DSR does increase with initial fuel thickness (ρR), for shots in which the shock timing and implosion velocity are kept fixed.

ACKNOWLEDGMENTS

We wish to thank the NIF operations team. This work was performed under the auspices of the U.S. Department of Energy by Lawrence Livermore National Laboratory under Contract DE-AC52-07NA27344 and by General Atomics under contract DE-NA0001808. The data that support the findings of this study are available from the corresponding author upon reasonable request. This document was prepared as an account of work sponsored by an agency of the United States government. Neither the United States government nor Lawrence Livermore National Security, LLC, nor any of their employees makes any warranty, expressed or implied, or assumes any legal liability or responsibility for the accuracy, completeness, or usefulness of any information, apparatus, product, or process disclosed, or represents that its use would not infringe privately owned rights. Reference herein to any specific commercial product, process, or service by trade

name, trademark, manufacturer, or otherwise does not necessarily constitute or imply its endorsement, recommendation, or favoring by the United States government or Lawrence Livermore National Security, LLC. The views and opinions of authors expressed herein do not necessarily state or reflect those of the United States government or Lawrence Livermore National Security, LLC, and shall not be used for advertising or product endorsement purposes.

REFERENCES

1. J. Lindl, Phys. Plasmas **2** (11), 3933-4024 (1995).

2. S. Atzeni and J. Meyer-ter-Vehn, *The Physics of Inertial Fusion*. (Oxford University Press, 2008).

3. K. L. Baker, C. A. Thomas, D. T. Casey, S. Khan, B. K. Spears, R. Nora, T. Woods, J. L. Milovich, R. L. Berger, D. Strozzi, D. Clark, M. Hohenberger, O. A. Hurricane, D. A. Callahan, O. L. Landen, B. Bachmann, R. Benedetti, R. Bionta, P. M. Celliers, D. Fittinghoff, C. Goyon, G. Grim, R. Hatarik, N. Izumi, M. Gatu Johnson, G. Kyrala, T. Ma, M. Millot, S. R. Nagel, A. Pak, P. K. Patel, D. Turnbull, P. L. Volegov and C. Yeamans, Phys Rev Lett **121** (13), 135001 (2018).

4. K. L. Baker, (LLNL, 2019).

5. M. C. Herrmann, M. Tabak and J. D. Lindl, Nuclear Fusion **41**, 99-111 (2001).

6. K. L. Baker, O. Jones, C. Weber, D. Clark, P. K. Patel, C. A. Thomas, O. L. Landen, R. Nora, G. J. Anderson, J. Gaffney, S. MacLaren, D. T. Casey, T. Döppner, E. L. Dewald, R. Tommasini, B. K. Spears, J. Salmonson, M. Hohenberger, S. Khan, A. Zylstra, A. Kritcher, P. Amendt, V. Smalyuk, J. Lindl, C. Young, J. S. Ross, D. Ho, O. A. Hurricane, D. A. Callahan, T. Woods, J. L. Milovich, D. J. Strozzi, B. Bachmann, R. Bionta, P. M. Celliers, D. Fittinghoff, R. Hatarik, M. Gatu Johnson, K. Meaney, M. Millot, P. L. Volegov and C. Wilde, Physics of Plasmas **29** (6), 062705 (2022).

7. K. L. Baker, S. MacLaren, O. Jones, B. K. Spears, P. K. Patel, R. Nora, L. Divol, O. L. Landen, G. J. Anderson, J. Gaffney, M. Kruse, O. A. Hurricane, D. A. Callahan, A. R. Christopherson, J. Salmonson, E. P. Hartouni, T. Döppner, E. Dewald, R. Tommasini, C. A.

Thomas, C. Weber, D. Clark, D. T. Casey, M. Hohenberger, S. Khan, T. Woods, J. L. Milovich, R. L. Berger, D. Strozzi, A. Kritcher, B. Bachmann, R. Benedetti, R. Bionta, P. M. Celliers, D. Fittinghoff, R. Hatarik, N. Izumi, M. Gatu Johnson, G. Kyrala, T. Ma, K. Meaney, M. Millot, S. R. Nagel, A. Pak, P. L. Volegov, C. Yeamans and C. Wilde, Physical Review E **107** (1), 015202 (2023).

8. K. L. Baker, C. A. Thomas, D. T. Casey, M. Hohenberger, S. Khan, B. K. Spears, O. L. Landen, R. Nora, D. T. Woods, J. L. Milovich, R. L. Berger, D. Strozzi, C. Weber, D. Clark, O. A. Hurricane, D. A. Callahan, A. L. Kritcher, B. Bachmann, L. R. Benedetti, R. Bionta, P. M. Celliers, D. Fittinghoff, C. Goyon, R. Hatarik, N. Izumi, M. Gatu Johnson, G. Kyrala, T. Ma, K. Meaney, M. Millot, S. R. Nagel, P. K. Patel, D. Turnbull, P. L. Volegov, C. Yeamans and C. Wilde, Phys Rev E **102** (2-1), 023210 (2020).

9. P. K. Patel, P. T. Springer, C. R. Weber, L. C. Jarrott, O. A. Hurricane, B. Bachmann, K. L. Baker, L. F. Berzak Hopkins, D. A. Callahan, D. T. Casey, C. J. Cerjan, D. S. Clark, E. L. Dewald, L. Divol, T. Döppner, J. E. Field, D. Fittinghoff, J. Gaffney, V. Geppert-Kleinrath, G. P. Grim, E. P. Hartouni, R. Hatarik, D. E. Hinkel, M. Hohenberger, K. Humbird, N. Izumi, O. S. Jones, S. F. Khan, A. L. Kritcher, M. Kruse, O. L. Landen, S. Le Pape, T. Ma, S. A. MacLaren, A. G. MacPhee, L. P. Masse, N. B. Meezan, J. L. Milovich, R. Nora, A. Pak, J. L. Peterson, J. Ralph, H. F. Robey, J. D. Salmonson, V. A. Smalyuk, B. K. Spears, C. A. Thomas, P. L. Volegov, A. Zylstra and M. J. Edwards, Physics of Plasmas **27** (5) (2020).

10. D. T. Casey, C. A. Thomas, K. L. Baker, B. K. Spears, M. Hohenberger, S. F. Khan, R. C. Nora, C. R. Weber, D. T. Woods, O. A. Hurricane, D. A. Callahan, R. L. Berger, J. L. Milovich, P. K. Patel, T. Ma, A. Pak, L. R. Benedetti, M. Millot, C. Jarrott, O. L. Landen, R. M. Bionta, B. J. MacGowan, D. J. Strozzi, M. Stadermann, J. Biener, A. Nikroo, C. S. Goyon, N. Izumi, S. R.

Nagel, B. Bachmann, P. L. Volegov, D. N. Fittinghoff, G. P. Grim, C. B. Yeamans, M. Gatu Johnson, J. A. Frenje, N. Rice, C. Kong, J. Crippen, J. Jaquez, K. Kangas and C. Wild, Physics of Plasmas **25** (5) (2018).

11. C. A. Thomas, E. M. Campbell, K. L. Baker, D. T. Casey, M. Hohenberger, A. L. Kritcher, B. K. Spears, S. F. Khan, R. Nora, D. T. Woods, J. L. Milovich, R. L. Berger, D. Strozzi, D. D. Ho, D. Clark, B. Bachmann, L. R. Benedetti, R. Bionta, P. M. Celliers, D. N. Fittinghoff, G. Grim, R. Hatarik, N. Izumi, G. Kyrala, T. Ma, M. Millot, S. R. Nagel, P. K. Patel, C. Yeamans, A. Nikroo, M. Tabak, M. Gatu Johnson, P. L. Volegov and S. M. Finnegan, Physics of Plasmas **27** (11) (2020).

12. C. A. Thomas, E. M. Campbell, K. L. Baker, D. T. Casey, M. Hohenberger, A. L. Kritcher, B. K. Spears, S. F. Khan, R. Nora, D. T. Woods, J. L. Milovich, R. L. Berger, D. Strozzi, D. D. Ho, D. Clark, B. Bachmann, L. R. Benedetti, R. Bionta, P. M. Celliers, D. N. Fittinghoff, G. Grim, R. Hatarik, N. Izumi, G. Kyrala, T. Ma, M. Millot, S. R. Nagel, P. K. Patel, C. Yeamans, A. Nikroo, M. Tabak, M. Gatu Johnson, P. L. Volegov and S. M. Finnegan, Physics of Plasmas **27**, 112712 (2020).

13. C. A. Thomas, E. M. Campbell, K. L. Baker, D. T. Casey, M. Hohenberger, A. L. Kritcher, B. K. Spears, S. F. Khan, R. Nora, D. T. Woods, J. L. Milovich, R. L. Berger, D. Strozzi, D. D. Ho, D. Clark, B. Bachmann, L. R. Benedetti, R. Bionta, P. M. Celliers, D. N. Fittinghoff, G. Grim, R. Hatarik, N. Izumi, G. Kyrala, T. Ma, M. Millot, S. R. Nagel, P. K. Patel, C. Yeamans, A. Nikroo, M. Tabak, M. Gatu Johnson, P. L. Volegov and S. M. Finnegan, Physics of Plasmas **27**, 112708 (2020).

14. M. Hohenberger, D. T. Casey, C. A. Thomas, O. L. Landen, K. L. Baker, L. R. Benedetti, D. A. Callahan, O. A. Hurricane, N. Izumi, S. F. Khan, T. Ma, D. A. Mariscal, S. R. Nagel, A. Pak and B. K. Spears, Physics of Plasmas **26** (11) (2019).

15. R. Berger, Thomas, Cliff A., K. Baker, D. Casey, C. Goyon, J. Park, N. Lemos, S. Khan, M. Hohenberger, J. Milovich, D. Strozzi, M. Belyaev, T. Chapman and A. B. Langdon, Physics of Plasmas **26**, 012709 (2019).

16. A. J. MacKinnon, N. B. Meezan, J. S. Ross, S. Le Pape, L. Berzak Hopkins, L. Divol, D. Ho, J. Milovich, A. Pak, J. Ralph, T. Döppner, P. K. Patel, C. Thomas, R. Tommasini, S. Haan, A. G. MacPhee, J. McNaney, J. Caggiano, R. Hatarik, R. Bionta, T. Ma, B. Spears, J. R. Rygg, L. R. Benedetti, R. P. J. Town, D. K. Bradley, E. L. Dewald, D. Fittinghoff, O. S. Jones, H. R. Robey, J. D. Moody, S. Khan, D. A. Callahan, A. Hamza, J. Biener, P. M. Celliers, D. G. Braun, D. J. Erskine, S. T. Prisbrey, R. J. Wallace, B. Kozioziemski, R. Dylla-Spears, J. Sater, G. Collins, E. Storm, W. Hsing, O. Landen, J. L. Atherton, J. D. Lindl, M. J. Edwards, J. A. Frenje, M. Gatu-Johnson, C. K. Li, R. Petrasso, H. Rinderknecht, M. Rosenberg, F. H. Séguin, A. Zylstra, J. P. Knauer, G. Grim, N. Guler, F. Merrill, R. Olson, G. A. Kyrala, J. D. Kilkenny, A. Nikroo, K. Moreno, D. E. Hoover, C. Wild and E. Werner, Physics of Plasmas **21** (5), 056318 (2014).

17. S. Le Pape, L. F. Berzak Hopkins, L. Divol, A. Pak, E. L. Dewald, S. Bhandarkar, L. R. Bennedetti, T. Bunn, J. Biener, J. Crippen, D. Casey, D. Edgell, D. N. Fittinghoff, M. Gatu-Johnson, C. Goyon, S. Haan, R. Hatarik, M. Havre, D. D. Ho, N. Izumi, J. Jaquez, S. F. Khan, G. A. Kyrala, T. Ma, A. J. Mackinnon, A. G. MacPhee, B. J. MacGowan, N. B. Meezan, J. Milovich, M. Millot, P. Michel, S. R. Nagel, A. Nikroo, P. Patel, J. Ralph, J. S. Ross, N. G. Rice, D. Strozzi, M. Stadermann, P. Volegov, C. Yeamans, C. Weber, C. Wild, D. Callahan and O. A. Hurricane, Phys Rev Lett **120** (24), 245003 (2018).

18. L. F. Berzak Hopkins, N. B. Meezan, S. Le Pape, L. Divol, A. J. Mackinnon, D. D. Ho, M. Hohenberger, O. S. Jones, G. Kyrala, J. L. Milovich, A. Pak, J. E. Ralph, J. S. Ross, L. R. Benedetti, J. Biener, R. Bionta, E. Bond, D. Bradley, J. Caggiano, D. Callahan, C. Cerjan, J.

Church, D. Clark, T. Doppner, R. Dylla-Spears, M. Eckart, D. Edgell, J. Field, D. N. Fittinghoff, M. Gatu Johnson, G. Grim, N. Guler, S. Haan, A. Hamza, E. P. Hartouni, R. Hatarik, H. W. Herrmann, D. Hinkel, D. Hoover, H. Huang, N. Izumi, S. Khan, B. Kozioziemski, J. Kroll, T. Ma, A. MacPhee, J. McNaney, F. Merrill, J. Moody, A. Nikroo, P. Patel, H. F. Robey, J. R. Rygg, J. Sater, D. Sayre, M. Schneider, S. Sepke, M. Stadermann, W. Stoeffl, C. Thomas, R. P. Town, P. L. Volegov, C. Wild, C. Wilde, E. Woerner, C. Yeamans, B. Yoxall, J. Kilkenny, O. L. Landen, W. Hsing and M. J. Edwards, Phys Rev Lett **114** (17), 175001 (2015).

19. N. B. Meezan, L. F. Berzak Hopkins, S. Le Pape, L. Divol, A. J. MacKinnon, T. Döppner, D. D. Ho, O. S. Jones, S. F. Khan, T. Ma, J. L. Milovich, A. E. Pak, J. S. Ross, C. A. Thomas, L. R. Benedetti, D. K. Bradley, P. M. Celliers, D. S. Clark, J. E. Field, S. W. Haan, N. Izumi, G. A. Kyrala, J. D. Moody, P. K. Patel, J. E. Ralph, J. R. Rygg, S. M. Sepke, B. K. Spears, R. Tommasini, R. P. J. Town, J. Biener, R. M. Bionta, E. J. Bond, J. A. Caggiano, M. J. Eckart, M. Gatu Johnson, G. P. Grim, A. V. Hamza, E. P. Hartouni, R. Hatarik, D. E. Hoover, J. D. Kilkenny, B. J. Kozioziemski, J. J. Kroll, J. M. McNaney, A. Nikroo, D. B. Sayre, M. Stadermann, C. Wild, B. E. Yoxall, O. L. Landen, W. W. Hsing and M. J. Edwards, Physics of Plasmas **22** (6) (2015).

20. D. D. M. Ho, S. W. Haan, J. D. Salmonson, D. S. Clark, J. D. Lindl, J. L. Milovich, C. A. Thomas, L. F. Berzak Hopkins and N. B. Meezan, Journal of Physics: Conference Series **717** (2016).

21. L. Divol, A. Pak, L. F. Berzak Hopkins, S. L. Pape, N. B. Meezan, E. L. Dewald, D. D. M. Ho, S. F. Khan, A. J. Mackinnon, J. S. Ross, D. P. Turnbull, C. Weber, P. M. Celliers, M. Millot, L. R. Benedetti, J. E. Field, N. Izumi, G. A. Kyrala, T. Ma, S. R. Nagel, J. R. Rygg, D. Edgell, A. G. Macphee, C. Goyon, M. Hohenberger, B. J. MacGowan, P. Michel, D. Strozzi, W. S. Cassata, D. Casey, D. N. Fittinghoff, N. Gharibyan, R. Hatarik, D. Sayre, P. Volegov, C. Yeamans, B.

Bachmann, T. Döppner, J. Biener, J. Crippen, C. Choate, H. Huang, C. Kong, A. Nikroo, N. G. Rice, M. Stadermann, S. D. Bhandarkar, S. Haan, B. Kozioziemski, W. W. Hsing, O. L. Landen, J. D. Moody, R. P. J. Town, D. A. Callahan, O. A. Hurricane and M. J. Edwards, Physics of Plasmas **24** (5), 056309 (2017).

22. J. D. Lindl, P. Amendt, R. L. Berger, S. G. Glendinning, S. H. Glenzer, S. W. Haan, R. L. Kauffman, O. L. Landen and L. J. Suter, Physics of Plasmas **11** (2), 339-491 (2004).

23. D. H. Cohen, O. L. Landen and J. J. MacFarlane, Physics of Plasmas **12** (2005).

24. G. B. Zimmerman and W. L. Kruer, Comments on Plasma Physics and Controlled Fusion **2**, 51-60 (1975).

25. J. A. Harte, W. E. Alley, D. S. Bailey, J. L. Eddleman and G. B. Zimmerman, 1996.

26. O. L. Landen, J. D. Lindl, S. W. Haan, D. T. Casey, P. M. Celliers, D. N. Fittinghoff, N. Gharibyan, V. N. Goncharov, G. P. Grim, E. P. Hartouni, O. A. Hurricane, B. J. MacGowan, S. A. MacLaren, K. D. Meaney, M. Millot, J. L. Milovich, P. K. Patel, H. S. Robey, P. T. Springer, P. L. Volegov and M. J. Edwards, Physics of Plasmas **28** (4) (2021).

27. R. E. Olson, G. A. Rochau, O. L. Landen and R. J. Leeper, Physics of Plasmas **18** (2011).

28. A. Casner, T. Jalinaud, L. Masse and D. Galmiche, Physics of Plasmas **22**, 100702 (2015).

29. N. B. Meezan, A. J. MacKinnon, D. G. Hicks, E. L. Dewald, R. Tommasini, S. Le Pape, T. Döppner, T. Ma, D. R. Farley, D. H. Kalantar, P. Di Nicola, D. A. Callahan, H. F. Robey, C. A. Thomas, S. T. Prisbrey, O. S. Jones, J. L. Milovich, D. S. Clark, D. C. Eder, M. B. Schneider, K. Widmann, J. A. Koch, J. D. Salmonson, Y. P. Opachich, L. R. Benedetti, S. F. Khan, A. G. MacPhee, S. M. Glenn, D. K. Bradley, E. G. Dzenitis, B. R. Nathan, J. J. Kroll, A. V. Hamza, S. N. Dixit, L. J. Atherton, O. L. Landen, S. H. Glenzer, W. W. Hsing, L. J. Suter, M. J. Edwards, B.

J. MacGowan, E. I. Moses, R. E. Olson, J. L. Kline, G. A. Kyrala, A. S. Moore, J. D. Kilkenny, A. Nikroo, K. Moreno and D. E. Hoover, Physics of Plasmas **20** (5), 056311 (2013).

30. J. D. Lindl, S. W. Haan, O. L. Landen, A. R. Christopherson and R. Betti, Physics of Plasmas **25** (12), 122704 (2018).

31. R. Betti, M. Umansky, V. Lobatchev, V. N. Goncharov and R. L. McCrory, Phys. Plasmas **8**, 5257 (2001).

32. R. Betti, K. Anderson, V. N. Goncharov, R. L. McCrory, D. D. Meyerhofer, S. Skupsky and R. P. J. Town, Physics of Plasmas **9** (5), 2277-2286 (2002).

33. J. D. Lindl, S. W. Haan and O. L. Landen, Physics of Plasmas **30**, 012705 (2023).

34. O. A. Hurricane, D. A. Callahan, D. T. Casey, P. M. Celliers, C. Cerjan, E. L. Dewald, T. R. Dittrich, T. Döppner, D. E. Hinkel, L. F. B. Hopkins, J. L. Kline, S. Le Pape, T. Ma, A. G. Macphee, J. L. Milovich, A. Pak, H. S. Park, P. K. Patel, B. A. Remington, J. D. Salmonson, P. T. Springer and R. Tommasini, Nature (2014).

35. P. K. Patel, to be submitted to Phys. Plasmas (2023).

36. Y. Saillard, Nuclear Fusion **46** (12), 1017-1035 (2006).

37. J. L. Kline, D. A. Callahan, S. H. Glenzer, N. B. Meezan, J. D. Moody, D. E. Hinkel, O. S. Jones, A. J. Mackinnon, R. Bennedetti, R. L. Berger, D. Bradley, E. L. Dewald, I. Bass, C. Bennett, M. Bowers, G. Brunton, J. Bude, S. Burkhart, A. Condor, J. M. Di Nicola, P. Di Nicola, S. N. Dixit, T. Doeppner, E. G. Dzenitis, G. Erbert, J. Folta, G. Grim, S. Glenn, A. Hamza, S. W. Haan, J. Heebner, M. Henesian, M. Hermann, D. G. Hicks, W. W. Hsing, N. Izumi, K. Jancaitis, O. S. Jones, D. Kalantar, S. F. Khan, R. Kirkwood, G. A. Kyrala, K. Lafortune, O. L. Landen, L. Lagin, D. Larson, S. L. Pape, T. Ma, A. G. Macphee, P. A. Michel, P. Miller, M. Montincelli, A. S. Moore, A. Nikroo, M. Nostrand, R. E. Olson, A. Pak, H. S. Park, J. P. Patel, L. Pelz, J. Ralph, S. P. Regan,

H. F. Robey, M. D. Rosen, J. S. Ross, M. B. Schneider, M. Shaw, V. A. Smalyuk, D. J. Strozzi, T. Suratwala, L. J. Suter, R. Tommasini, R. P. J. Town, B. Van Wonterghem, P. Wegner, K. Widmann, C. Widmayer, H. Wilkens, E. A. Williams, M. J. Edwards, B. A. Remington, B. J. Macgowan, J. D. Kilkenny, J. D. Lindl, L. J. Atherton, S. H. Batha and E. Moses, Physics of Plasmas **20** (2013).

38. J. Lindl, O. Landen, J. Edwards and E. Moses, Phys. Plasmas **21** (2), 020501 (2014).

39. T. Döppner, D. E. Hinkel, L. C. Jarrott, L. Masse, J. E. Ralph, L. R. Benedetti, B. Bachmann, P. M. Celliers, D. T. Casey, L. Divol, J. E. Field, C. Goyon, R. Hatarik, M. Hohenberger, N. Izumi, S. F. Khan, A. L. Kritcher, T. Ma, B. J. MacGowan, M. Millot, J. Milovich, S. Nagel, A. Pak, J. Park, P. Patel, R. Tommasini, P. Volegov, C. Weber, O. L. Landen, D. A. Callahan, O. A. Hurricane and M. J. Edwards, Physics of Plasmas **27** (4), 042701 (2020).

40. D. A. Callahan, O. A. Hurricane, J. E. Ralph, C. A. Thomas, K. L. Baker, L. R. Benedetti, L. F. Berzak Hopkins, D. T. Casey, T. Chapman, C. E. Czajka, E. L. Dewald, L. Divol, T. Döppner, D. E. Hinkel, M. Hohenberger, L. C. Jarrott, S. F. Khan, A. L. Kritcher, O. L. Landen, S. LePape, S. A. MacLaren, L. P. Masse, N. B. Meezan, A. E. Pak, J. D. Salmonson, D. T. Woods, N. Izumi, T. Ma, D. A. Mariscal, S. R. Nagel, J. L. Kline, G. A. Kyrala, E. N. Loomis, S. A. Yi, A. B. Zylstra and S. H. Batha, Physics of Plasmas **25** (5), 056305 (2018).

41. N. Izumi, D. T. Woods, N. B. Meezan, J. D. Moody, O. L. Landen, L. Divol, H. Chen, D. A. Callahan, M. Hohenberger, A. L. Kritcher, D. T. Casey, M. D. Rosen, J. S. Ross, M. B. Schneider, M. J. Edwards and W. W. Hsing, Physics of Plasmas **28** (2), 022706 (2021).

42. R. E. Turner, P. Amendt, O. L. Landen, S. G. Glendinning, P. Bell, C. Decker, B. A. Hammel, D. Kalantar, D. Lee, R. Wallace, D. Bradley, M. Cable, R. S. Craxton, R. Kremens, W.

Seka, J. Schnittman, K. Thorp, T. J. Murphy, N. Delamater, C. W. Barnes, A. Hauer, G. Magelssen and J. Wallace, Physics of Plasmas **7** (1), 333-337 (2000).

43. J. Ralph, P. Michel, A. Kemp, D. Strozzi, B. MacGowan, N. Meezan, O. Landen, J.-M. DiNicola, N. Lemos, M. Belyaev, R. Berger, D. Callahan, T. Chapman, L. Divol, D. Hinkel, J. Moody, O. Jones, M. Stadermann and A. Nikroo, 2020 (unpublished).

44. A. B. Zylstra, A. L. Kritcher, O. A. Hurricane, D. A. Callahan, K. Baker, T. Braun, D. T. Casey, D. Clark, K. Clark, T. Doppner, L. Divol, D. E. Hinkel, M. Hohenberger, C. Kong, O. L. Landen, A. Nikroo, A. Pak, P. Patel, J. E. Ralph, N. Rice, R. Tommasini, M. Schoff, M. Stadermann, D. Strozzi, C. Weber, C. Young, C. Wild, R. P. J. Town and M. J. Edwards, PHYSICAL REVIEW LETTERS **126** (2021).

45. A. L. Kritcher, A. B. Zylstra, D. A. Callahan, O. A. Hurricane, C. Weber, J. Ralph, D. T. Casey, A. Pak, K. Baker, B. Bachmann, S. Bhandarkar, J. Biener, R. Bionta, T. Braun, M. Bruhn, C. Choate, D. Clark, J. M. Di Nicola, L. Divol, T. Doeppner, V. Geppert-Kleinrath, S. Haan, J. Heebner, V. Hernandez, D. Hinkel, M. Hohenberger, H. Huang, C. Kong, S. Le Pape, D. Mariscal, E. Marley, L. Masse, K. D. Meaney, M. Millot, A. Moore, K. Newman, A. Nikroo, P. Patel, L. Pelz, N. Rice, H. Robey, J. S. Ross, M. Rubery, J. Salmonson, D. Schlossberg, S. Sepke, K. Sequoia, M. Stadermann, D. Strozzi, R. Tommasini, P. Volegov, C. Wild, S. Yang, C. Young, M. J. Edwards, O. Landen, R. Town and M. Herrmann, Physics of Plasmas **28** (7) (2021).

46. A. L. Kritcher, D. T. Casey, C. A. Thomas, A. B. Zylstra, M. Hohenberger, K. Baker, S. Le Pape, B. Bachmann, S. Bhandarkar, J. Biener, T. Braun, D. Clark, L. Divol, T. Döppner, D. Hinkel, C. Kong, D. Mariscal, M. Millot, J. Milovich, A. Nikroo, A. Pak, N. Rice, H. Robey, M. Stadermann, J. Sevier, D. Strozzi, C. Weber, C. Wild, B. Woodworth, J. Edwards, D. A. Callahan and O. A. Hurricane, Physics of Plasmas **27** (5) (2020).

47. M. Hohenberger, D. T. Casey, A. L. Kritcher, A. Pak, A. B. Zylstra, C. A. Thomas, K. L. Baker, S. Le Pape, B. Bachmann, R. L. Berger, J. Biener, D. S. Clark, L. Divol, T. Döppner, V. Geppert-Kleinrath, D. Hinkel, H. Huang, C. Kong, O. L. Landen, J. Milovich, A. Nikroo, N. Rice, H. Robey, M. Schoff, J. Sevier, K. Sequoia, M. Stadermann, D. Strozzi, P. L. Volegov, C. Weber, C. Wild, B. Woodworth, D. A. Callahan and O. A. Hurricane, Physics of Plasmas **27** (11) (2020).

48. V. A. Smalyuk, C. R. Weber, H. F. Robey, D. T. Casey, K.-C. Chen, D. S. Clark, M. Farrell, S. Felker, J. E. Field, S. W. Haan, B. A. Hammel, A. V. Hamza, D. Hoover, J. J. Kroll, O. L. Landen, A. G. MacPhee, D. Martinez, A. Nikroo and N. Rice, Physics of Plasmas **24** (2017).

49. O. A. Hurricane, D. A. Callahan, D. T. Casey, E. L. Dewald, T. R. Dittrich, T. Döppner, M. A. Barrios Garcia, D. E. Hinkel, L. F. Berzak Hopkins, P. Kervin, J. L. Kline, S. L. Pape, T. Ma, A. G. MacPhee, J. L. Milovich, J. Moody, A. E. Pak, P. K. Patel, H. S. Park, B. A. Remington, H. F. Robey, J. D. Salmonson, P. T. Springer, R. Tommasini, L. R. Benedetti, J. A. Caggiano, P. Celliers, C. Cerjan, R. Dylla-Spears, D. Edgell, M. J. Edwards, D. Fittinghoff, G. P. Grim, N. Guler, N. Izumi, J. A. Frenje, M. Gatu Johnson, S. Haan, R. Hatarik, H. Herrmann, S. Khan, J. Knauer, B. J. Kozioziemski, A. L. Kritcher, G. Kyrala, S. A. Maclaren, F. E. Merrill, P. Michel, J. Ralph, J. S. Ross, J. R. Rygg, M. B. Schneider, B. K. Spears, K. Widmann and C. B. Yeamans, Physics of Plasmas **21** (5) (2014).

50. H. S. Park, O. A. Hurricane, D. A. Callahan, D. T. Casey, E. L. Dewald, T. R. Dittrich, T. Döppner, D. E. Hinkel, L. F. Berzak Hopkins, S. Le Pape, T. Ma, P. K. Patel, B. A. Remington, H. F. Robey, J. D. Salmonson and J. L. Kline, Physical Review Letters, 055001 (2014).

51. T. R. Dittrich, O. A. Hurricane, D. A. Callahan, E. L. Dewald, T. Döppner, D. E. Hinkel, L. F. Berzak Hopkins, S. Le Pape, T. Ma, J. L. Milovich, J. C. Moreno, P. K. Patel, H. S. Park, B. A. Remington, J. D. Salmonson and J. L. Kline, Physical Review Letters **112**, 055002 (2014).

52. D. E. Hinkel, T. Döppner, L. P. Masse, K. Widmann, L. Divol, B. Bachmann, L. F. Berzak Hopkins, S. LePape, C. R. Weber, S. A. MacLaren, A. B. Zylstra, J. E. Ralph, L. R. Benedetti, A. S. Moore, C. A. Thomas, D. T. Casey, V. A. Smalyuk, H. F. Robey, P. M. Celliers, M. J. MacDonald, C. M. Krauland, D. B. Thorn, M. D. Rosen, P. K. Patel, B. J. MacGowan, M. B. Schneider, D. S. Clark, A. E. Pak, M. J. Edwards, O. L. Landen, D. A. Callahan and O. A. Hurricane, High Energy Density Physics **37**, 100884 (2020).

53. K. L. Baker, H. F. Robey, J. L. Milovich, O. S. Jones, V. A. Smalyuk, D. T. Casey, A. G. MacPhee, A. Pak, P. M. Celliers, D. S. Clark, O. L. Landen, J. L. Peterson, L. F. Berzak-Hopkins, C. R. Weber, S. W. Haan, T. D. Döppner, S. Dixit, E. Giraldez, A. V. Hamza, K. S. Jancaitis, J. J. Kroll, K. N. Lafortune, B. J. MacGowan, J. D. Moody, A. Nikroo and C. C. Widmayer, Physics of Plasmas **22** (5), 052702 (2015).

54. D. T. Casey, J. L. Milovich, V. A. Smalyuk, D. S. Clark, H. F. Robey, A. Pak, A. G. MacPhee, K. L. Baker, C. R. Weber, T. Ma, H. S. Park, T. Doppner, D. A. Callahan, S. W. Haan, P. K. Patel, J. L. Peterson, D. Hoover, A. Nikroo, C. B. Yeamans, F. E. Merrill, P. L. Volegov, D. N. Fittinghoff, G. P. Grim, M. J. Edwards, O. L. Landen, K. N. Lafortune, B. J. MacGowan, C. C. Widmayer, D. B. Sayre, R. Hatarik, E. J. Bond, S. R. Nagel, L. R. Benedetti, N. Izumi, S. Khan, B. Bachmann, B. K. Spears, C. J. Cerjan, M. Gatu Johnson and J. A. Frenje, Phys Rev Lett **115** (10), 105001 (2015).

55. V. A. Smalyuk, H. F. Robey, T. Döppner, D. T. Casey, D. S. Clark, O. S. Jones, J. L. Milovich, J. L. Peterson, B. Bachmann, K. L. Baker, L. R. Benedetti, L. F. Berzak Hopkins, R. Bionta, E. Bond, D. K. Bradley, D. A. Callahan, P. M. Celliers, C. Cerjan, K.-C. Chen, C. Goyon, G. Grim, S. N. Dixit, M. J. Eckart, M. J. Edwards, M. Farrell, D. N. Fittinghoff, J. A. Frenje, M. Gatu-Johnson, N. Gharibyan, S. W. Haan, A. V. Hamza, E. Hartouni, R. Hatarik, M. Havre, M.

Hohenberger, D. Hoover, O. A. Hurricane, N. Izumi, K. S. Jancaitis, S. F. Khan, J. P. Knauer, J. J. Kroll, G. Kyrala, K. N. LaFortune, O. L. Landen, T. Ma, B. J. MacGowan, A. G. MacPhee, M. Mauldin, F. E. Merrill, A. S. Moore, S. Nagel, A. Nikroo, A. Pak, P. K. Patel, J. E. Ralph, D. B. Sayre, D. Shaughnessy, B. K. Spears, R. Tommasini, D. P. Turnbull, A. L. Velikovich, P. L. Volegov, C. R. Weber, C. C. Widmayer and C. Yeamans, Physics of Plasmas **23**, 102703 (2016).

56. H. F. Robey, L. Berzak Hopkins, J. L. Milovich and N. B. Meezan, Physics of Plasmas **25** (1) (2018).

57. A. B. Zylstra, A. L. Kritcher, O. A. Hurricane, D. A. Callahan, J. E. Ralph, D. T. Casey, A. Pak, O. L. Landen, B. Bachmann, K. L. Baker, L. Berzak Hopkins, S. D. Bhandarkar, J. Biener, R. M. Bionta, N. W. Birge, T. Braun, T. M. Briggs, P. M. Celliers, H. Chen, C. Choate, D. S. Clark, L. Divol, T. Döppner, D. Fittinghoff, M. J. Edwards, M. Gatu Johnson, N. Gharibyan, S. Haan, K. D. Hahn, E. Hartouni, D. E. Hinkel, D. D. Ho, M. Hohenberger, J. P. Holder, H. Huang, N. Izumi, J. Jeet, O. Jones, S. M. Kerr, S. F. Khan, H. Geppert Kleinrath, V. Geppert Kleinrath, C. Kong, K. M. Lamb, S. Le Pape, N. C. Lemos, J. D. Lindl, B. J. MacGowan, A. J. Mackinnon, A. G. MacPhee, E. V. Marley, K. Meaney, M. Millot, A. S. Moore, K. Newman, J. M. G. Di Nicola, A. Nikroo, R. Nora, P. K. Patel, N. G. Rice, M. S. Rubery, J. Sater, D. J. Schlossberg, S. M. Sepke, K. Sequoia, S. J. Shin, M. Stadermann, S. Stoupin, D. J. Strozzi, C. A. Thomas, R. Tommasini, C. Trosseille, E. R. Tubman, P. L. Volegov, C. R. Weber, C. Wild, D. T. Woods, S. T. Yang and C. V. Young, Physical Review E **106** (2) (2022).

58. A. L. Kritcher, A. B. Zylstra, D. A. Callahan, O. A. Hurricane, C. R. Weber, D. S. Clark, C. V. Young, J. E. Ralph, D. T. Casey, A. Pak, O. L. Landen, B. Bachmann, K. L. Baker, L. Berzak Hopkins, S. D. Bhandarkar, J. Biener, R. M. Bionta, N. W. Birge, T. Braun, T. M. Briggs, P. M. Celliers, H. Chen, C. Choate, L. Divol, T. Döppner, D. Fittinghoff, M. J. Edwards, M. Gatu

Johnson, N. Gharibyan, S. Haan, K. D. Hahn, E. Hartouni, D. E. Hinkel, D. D. Ho, M. Hohenberger, J. P. Holder, H. Huang, N. Izumi, J. Jeet, O. Jones, S. M. Kerr, S. F. Khan, H. Geppert Kleinrath, V. Geppert Kleinrath, C. Kong, K. M. Lamb, S. Le Pape, N. C. Lemos, J. D. Lindl, B. J. MacGowan, A. J. Mackinnon, A. G. MacPhee, E. V. Marley, K. Meaney, M. Millot, A. S. Moore, K. Newman, J. M. G. Di Nicola, A. Nikroo, R. Nora, P. K. Patel, N. G. Rice, M. S. Rubery, J. Sater, D. J. Schlossberg, S. M. Sepke, K. Sequoia, S. J. Shin, M. Stadermann, S. Stoupin, D. J. Strozzi, C. A. Thomas, R. Tommasini, C. Trosseille, E. R. Tubman, P. L. Volegov, C. Wild, D. T. Woods and S. T. Yang, Physical Review E **106** (2), 025201 (2022).

59. H. Abu-Shawareb, R. Acree, P. Adams, J. Adams, B. Addis, R. Aden, P. Adrian, B. B. Afeyan, M. Aggleton, L. Aghaian, A. Aguirre, D. Aikens, J. Akre, F. Albert, M. Albrecht, B. J. Albright, J. Albritton, J. Alcala, C. Alday, D. A. Alessi, N. Alexander, J. Alfonso, N. Alfonso, E. Alger, S. J. Ali, Z. A. Ali, W. E. Alley, P. Amala, P. A. Amendt, P. Amick, S. Ammula, C. Amorin, D. J. Ampleford, R. W. Anderson, T. Anklam, N. Antipa, B. Appelbe, C. Aracne-Ruddle, E. Araya, M. Arend, P. Arnold, T. Arnold, J. Asay, L. J. Atherton, D. Atkinson, R. Atkinson, J. M. Auerbach, B. Austin, L. Auyang, A. S. Awwal, J. Ayers, S. Ayers, T. Ayers, S. Azevedo, B. Bachmann, C. A. Back, J. Bae, D. S. Bailey, J. Bailey, T. Baisden, K. L. Baker, H. Baldis, D. Barber, M. Barberis, D. Barker, A. Barnes, C. W. Barnes, M. A. Barrios, C. Barty, I. Bass, S. H. Batha, S. H. Baxamusa, G. Bazan, J. K. Beagle, R. Beale, B. R. Beck, J. B. Beck, M. Bedzyk, R. G. Beeler, R. G. Beeler, W. Behrendt, L. Belk, P. Bell, M. Belyaev, J. F. Benage, G. Bennett, L. R. Benedetti, L. X. Benedict, R. Berger, T. Bernat, L. A. Bernstein, B. Berry, L. Bertolini, G. Besenbruch, J. Betcher, R. Bettenhausen, R. Betti, B. Bezzerides, S. D. Bhandarkar, R. Bickel, J. Biener, T. Biesiada, K. Bigelow, J. Bigelow-Granillo, V. Bigman, R. M. Bionta, N. W. Birge, M. Bitter, A. C. Black, R. Bleile, D. L. Bleuel, E. Bliss, E. Bliss, B. Blue, T. Boehly, K. Boehm, C. D. Boley, R. Bonanno,

E. J. Bond, T. Bond, M. J. Bonino, M. Borden, J. L. Bourgade, J. Bousquet, J. Bowers, M. Bowers, R. Boyd, A. Bozek, D. K. Bradley, K. S. Bradley, P. A. Bradley, L. Bradley, L. Brannon, P. S. Brantley, D. Braun, T. Braun, K. Brienza-Larsen, T. M. Briggs, J. Britten, E. D. Brooks, D. Browning, M. W. Bruhn, T. A. Brunner, H. Bruns, G. Brunton, B. Bryant, T. Buczek, J. Bude, L. Buitano, S. Burkhart, J. Burmark, A. Burnham, R. Burr, L. E. Busby, B. Butlin, R. Cabeltis, M. Cable, W. H. Cabot, B. Cagadas, J. Caggiano, R. Cahayag, S. E. Caldwell, S. Calkins, D. A. Callahan, J. Calleja-Aguirre, L. Camara, D. Camp, E. M. Campbell, J. H. Campbell, B. Carey, R. Carey, K. Carlisle, L. Carlson, L. Carman, J. Carmichael, A. Carpenter, C. Carr, J. A. Carrera, D. Casavant, A. Casey, D. T. Casey, A. Castillo, E. Castillo, J. I. Castor, C. Castro, W. Caughey, R. Cavitt, J. Celeste, P. M. Celliers, C. Cerjan, G. Chandler, B. Chang, C. Chang, J. Chang, L. Chang, R. Chapman, T. Chapman, L. Chase, H. Chen, H. Chen, K. Chen, L. Y. Chen, B. Cheng, J. Chittenden, C. Choate, J. Chou, R. E. Chrien, M. Chrisp, K. Christensen, M. Christensen, A. R. Christopherson, M. Chung, J. A. Church, A. Clark, D. S. Clark, K. Clark, R. Clark, L. Claus, B. Cline, J. A. Cline, J. A. Cobble, K. Cochrane, B. Cohen, S. Cohen, M. R. Collette, G. Collins, L. A. Collins, T. J. B. Collins, A. Conder, B. Conrad, M. Conyers, A. W. Cook, D. Cook, R. Cook, J. C. Cooley, G. Cooper, T. Cope, S. R. Copeland, F. Coppari, J. Cortez, J. Cox, D. H. Crandall, J. Crane, R. S. Craxton, M. Cray, A. Crilly, J. W. Crippen, D. Cross, M. Cuneo, G. Cuotts, C. E. Czajka, D. Czechowicz, T. Daly, P. Danforth, R. Darbee, B. Darlington, P. Datte, L. Dauffy, G. Davalos, S. Davidovits, P. Davis, J. Davis, S. Dawson, R. D. Day, T. H. Day, M. Dayton, C. Deck, C. Decker, C. Deeney, K. A. DeFriend, G. Deis, N. D. Delamater, J. A. Delettrez, R. Demaret, S. Demos, S. M. Dempsey, R. Desjardin, T. Desjardins, M. P. Desjarlais, E. L. Dewald, J. DeYoreo, S. Diaz, G. Dimonte, T. R. Dittrich, L. Divol, S. N. Dixit, J. Dixon, E. S. Dodd, D. Dolan, A. Donovan, M. Donovan, T. Doppner, C. Dorrer, N. Dorsano, M. R. Douglas, D. Dow, J. Downie,

E. Downing, M. Dozieres, V. Draggoo, D. Drake, R. P. Drake, T. Drake, G. Dreifuerst, D. F. DuBois, P. F. DuBois, G. Dunham, R. Dylla-Spears, A. K. L. Dymoke-Bradshaw, B. Dzenitis, C. Ebbers, M. Eckart, S. Eddinger, D. Eder, D. Edgell, M. J. Edwards, P. Efthimion, J. H. Eggert, B. Ehrlich, P. Ehrmann, S. Elhadj, C. Ellerbee, N. S. Elliott, C. L. Ellison, F. Elsner, M. Emerich, K. Engelhorn, T. England, E. English, P. Epperson, R. Epstein, G. Erbert, M. A. Erickson, D. J. Erskine, A. Erlandson, R. J. Espinosa, C. Estes, K. G. Estabrook, S. Evans, A. Fabyan, J. Fair, R. Fallejo, N. Farmer, W. A. Farmer, M. Farrell, V. E. Fatherley, M. Fedorov, E. Feigenbaum, M. Feit, W. Ferguson, J. C. Fernandez, A. Fernandez-Panella, S. Fess, J. E. Field, C. V. Filip, J. R. Fincke, T. Finn, S. M. Finnegan, R. G. Finucane, M. Fischer, A. Fisher, J. Fisher, B. Fishler, D. Fittinghoff, P. Fitzsimmons, M. Flegel, K. A. Flippo, J. Florio, J. Folta, P. Folta, L. R. Foreman, C. Forrest, A. Forsman, J. Fooks, M. Foord, R. Fortner, K. Fournier, D. E. Fratanduono, N. Frazier, T. Frazier, C. Frederick, M. S. Freeman, J. Frenje, D. Frey, G. Frieders, S. Friedrich, D. H. Froula, J. Fry, T. Fuller, J. Gaffney, S. Gales, B. Le Galloudec, K. K. Le Galloudec, A. Gambhir, L. Gao, W. J. Garbett, A. Garcia, C. Gates, E. Gaut, P. Gauthier, Z. Gavin, J. Gaylord, M. Geissel, F. Genin, J. Georgeson, H. Geppert-Kleinrath, V. Geppert-Kleinrath, N. Gharibyan, J. Gibson, C. Gibson, E. Giraldez, V. Glebov, S. G. Glendinning, S. Glenn, S. H. Glenzer, S. Goade, P. L. Gobby, S. R. Goldman, B. Golick, M. Gomez, V. Goncharov, D. Goodin, P. Grabowski, E. Grafil, P. Graham, J. Grandy, E. Grasz, F. Graziani, G. Greenman, J. A. Greenough, A. Greenwood, G. Gregori, T. Green, J. R. Griego, G. P. Grim, J. Grondalski, S. Gross, J. Guckian, N. Guler, B. Gunney, G. Guss, S. Haan, J. Hackbarth, L. Hackel, R. Hackel, C. Haefner, C. Hagmann, K. D. Hahn, S. Hahn, B. J. Haid, B. M. Haines, B. M. Hall, C. Hall, G. N. Hall, M. Hamamoto, S. Hamel, C. E. Hamilton, B. A. Hammel, J. H. Hammer, G. Hampton, A. Hamza, A. Handler, S. Hansen, D. Hanson, R. Haque, D. Harding, E. Harding, J. D. Hares, D. B. Harris, J. A. Harte, E. P. Hartouni,

R. Hatarik, S. Hatchett, A. A. Hauer, M. Havre, R. Hawley, J. Hayes, J. Hayes, S. Hayes, A. Hayes-Sterbenz, C. A. Haynam, D. A. Haynes, D. Headley, A. Heal, J. E. Heebner, S. Heerey, G. M. Heestand, R. Heeter, N. Hein, C. Heinbockel, C. Hendricks, M. Henesian, J. Heninger, J. Henrikson, E. A. Henry, E. B. Herbold, M. R. Hermann, G. Hermes, J. E. Hernandez, V. J. Hernandez, M. C. Herrmann, H. W. Herrmann, O. D. Herrera, D. Hewett, R. Hibbard, D. G. Hicks, D. Hill, K. Hill, T. Hilsabeck, D. E. Hinkel, D. D. Ho, V. K. Ho, J. K. Hoffer, N. M. Hoffman, M. Hohenberger, M. Hohensee, W. Hoke, D. Holdener, F. Holdener, J. P. Holder, B. Holko, D. Holunga, J. F. Holzrichter, J. Honig, D. Hoover, D. Hopkins, L. Berzak Hopkins, M. Hoppe, M. L. Hoppe, J. Horner, R. Hornung, C. J. Horsfield, J. Horvath, D. Hotaling, R. House, L. Howell, W. W. Hsing, S. X. Hu, H. Huang, J. Huckins, H. Hui, K. D. Humbird, J. Hund, J. Hunt, O. A. Hurricane, M. Hutton, K. H. Huynh, L. Inandan, C. Iglesias, I. V. Igumenshchev, N. Izumi, M. Jackson, J. Jackson, S. D. Jacobs, G. James, K. Jancaitis, J. Jarboe, L. C. Jarrott, D. Jasion, J. Jaquez, J. Jeet, A. E. Jenei, J. Jensen, J. Jimenez, R. Jimenez, D. Jobe, Z. Johal, H. M. Johns, D. Johnson, M. A. Johnson, M. Gatu Johnson, R. J. Johnson, S. Johnson, S. A. Johnson, T. Johnson, K. Jones, O. Jones, M. Jones, R. Jorge, H. J. Jorgenson, M. Julian, B. I. Jun, R. Jungquist, J. Kaae, N. Kabadi, D. Kaczala, D. Kalantar, K. Kangas, V. V. Karasiev, M. Karasik, V. Karpenko, A. Kasarky, K. Kasper, R. Kauffman, M. I. Kaufman, C. Keane, L. Keaty, L. Kegelmeyer, P. A. Keiter, P. A. Kellett, J. Kellogg, J. H. Kelly, S. Kemic, A. J. Kemp, G. E. Kemp, G. D. Kerbel, D. Kershaw, S. M. Kerr, T. J. Kessler, M. H. Key, S. F. Khan, H. Khater, C. Kiikka, J. Kilkenny, Y. Kim, Y. J. Kim, J. Kimko, M. Kimmel, J. M. Kindel, J. King, R. K. Kirkwood, L. Klaus, D. Klem, J. L. Kline, J. Klingmann, G. Kluth, P. Knapp, J. Knauer, J. Knipping, M. Knudson, D. Kobs, J. Koch, T. Kohut, C. Kong, J. M. Koning, P. Koning, S. Konior, H. Kornblum, L. B. Kot, B. Kozioziemski, M. Kozlowski, P. M. Kozlowski, J. Krammen, N. S. Krasheninnikova, B. Kraus,

W. Krauser, J. D. Kress, A. L. Kritcher, E. Krieger, J. J. Kroll, W. L. Kruer, M. K. G. Kruse, S. Kucheyev, M. Kumbera, S. Kumpan, J. Kunimune, B. Kustowski, T. J. T. Kwan, G. A. Kyrala, S. Laffite, M. Lafon, K. LaFortune, B. Lahmann, B. Lairson, O. L. Landen, J. Langenbrunner, L. Lagin, T. Land, M. Lane, D. Laney, A. B. Langdon, S. H. Langer, A. Langro, N. E. Lanier, T. E. Lanier, D. Larson, B. F. Lasinski, D. Lassle, D. LaTray, G. Lau, N. Lau, C. Laumann, A. Laurence, T. A. Laurence, J. Lawson, H. P. Le, R. R. Leach, L. Leal, A. Leatherland, K. LeChien, B. Lechleiter, A. Lee, M. Lee, T. Lee, R. J. Leeper, E. Lefebvre, J. P. Leidinger, B. LeMire, R. W. Lemke, N. C. Lemos, S. Le Pape, R. Lerche, S. Lerner, S. Letts, K. Levedahl, T. Lewis, C. K. Li, H. Li, J. Li, W. Liao, Z. M. Liao, D. Liedahl, J. Liebman, G. Lindford, E. L. Lindman, J. D. Lindl, H. Loey, R. A. London, F. Long, E. N. Loomis, F. E. Lopez, H. Lopez, E. Losbanos, S. Loucks, R. Lowe-Webb, E. Lundgren, A. P. Ludwigsen, R. Luo, J. Lusk, R. Lyons, T. Ma, Y. Macallop, M. J. MacDonald, B. J. MacGowan, J. M. Mack, A. J. Mackinnon, S. A. MacLaren, A. G. MacPhee, G. R. Magelssen, J. Magoon, R. M. Malone, T. Malsbury, R. Managan, R. Mancini, K. Manes, D. Maney, D. Manha, O. M. Mannion, A. M. Manuel, E. Mapoles, G. Mara, T. Marcotte, E. Marin, M. M. Marinak, C. Mariscal, D. A. Mariscal, E. F. Mariscal, E. V. Marley, J. A. Marozas, R. Marquez, C. D. Marshall, F. J. Marshall, M. Marshall, S. Marshall, J. Marticorena, D. Martinez, I. Maslennikov, D. Mason, R. J. Mason, L. Masse, W. Massey, P. E. Masson-Laborde, N. D. Masters, D. Mathisen, E. Mathison, J. Matone, M. J. Matthews, C. Mattoon, T. R. Mattsson, K. Matzen, C. W. Mauche, M. Mauldin, T. McAbee, M. McBurney, T. McCarville, R. L. McCrory, A. M. McEvoy, C. McGuffey, M. McInnis, P. McKenty, M. S. McKinley, J. B. McLeod, A. McPherson, B. McQuillan, M. Meamber, K. D. Meaney, N. B. Meezan, R. Meissner, T. A. Mehlhorn, N. C. Mehta, J. Menapace, F. E. Merrill, B. T. Merritt, E. C. Merritt, D. D. Meyerhofer, S. Mezyk, R. J. Mich, P. A. Michel, D. Milam, C. Miller, D. Miller, D. S. Miller, E. Miller, E. K.

Miller, J. Miller, M. Miller, P. E. Miller, T. Miller, W. Miller, V. Miller-Kamm, M. Millot, J. L. Milovich, P. Minner, J. L. Miquel, S. Mitchell, K. Molvig, R. C. Montesanti, D. S. Montgomery, M. Monticelli, A. Montoya, J. D. Moody, A. S. Moore, E. Moore, M. Moran, J. C. Moreno, K. Moreno, B. E. Morgan, T. Morrow, J. W. Morton, E. Moses, K. Moy, R. Muir, M. S. Murillo, J. E. Murray, J. R. Murray, D. H. Munro, T. J. Murphy, F. M. Munteanu, J. Nafziger, T. Nagayama, S. R. Nagel, R. Nast, R. A. Negres, A. Nelson, D. Nelson, J. Nelson, S. Nelson, S. Nemethy, P. Neumayer, K. Newman, M. Newton, H. Nguyen, J. G. Di Nicola, P. Di Nicola, C. Niemann, A. Nikroo, P. M. Nilson, A. Nobile, V. Noorai, R. Nora, M. Norton, M. Nostrand, V. Note, S. Novell, P. F. Nowak, A. Nunez, R. A. Nyholm, M. O'Brien, A. Oceguera, J. A. Oertel, J. Okui, B. Olejniczak, J. Oliveira, P. Olsen, B. Olson, K. Olson, R. E. Olson, Y. P. Opachich, N. Orsi, C. D. Orth, M. Owen, S. Padalino, E. Padilla, R. Paguio, S. Paguio, J. Paisner, S. Pajoom, A. Pak, S. Palaniyappan, K. Palma, T. Pannell, F. Papp, D. Paras, T. Parham, H. S. Park, A. Pasternak, S. Patankar, M. V. Patel, P. K. Patel, R. Patterson, S. Patterson, B. Paul, M. Paul, E. Pauli, O. T. Pearce, J. Pearcy, B. Pedrotti, A. Peer, L. J. Pelz, B. Penetrante, J. Penner, A. Perez, L. J. Perkins, E. Pernice, T. S. Perry, S. Person, D. Petersen, T. Petersen, D. L. Peterson, E. B. Peterson, J. E. Peterson, J. L. Peterson, K. Peterson, R. R. Peterson, R. D. Petrasso, F. Philippe, T. J. Phipps, E. Piceno, Y. Ping, L. Pickworth, J. Pino, R. Plummer, G. D. Pollack, S. M. Pollaine, B. B. Pollock, D. Ponce, J. Ponce, J. Pontelandolfo, J. L. Porter, J. Post, O. Poujade, C. Powell, H. Powell, G. Power, M. Pozulp, M. Prantil, M. Prasad, S. Pratuch, S. Price, K. Primdahl, S. Prisbrey, R. Procassini, A. Pruyne, B. Pudliner, S. R. Qiu, K. Quan, M. Quinn, J. Quintenz, P. B. Radha, F. Rainer, J. E. Ralph, K. S. Raman, R. Raman, P. Rambo, S. Rana, A. Randewich, D. Rardin, M. Ratledge, N. Ravelo, F. Ravizza, M. Rayce, A. Raymond, B. Raymond, B. Reed, C. Reed, S. Regan, B. Reichelt, V. Reis, S. Reisdorf, V. Rekow, B. A. Remington, A. Rendon, W. Requieron,

M. Rever, H. Reynolds, J. Reynolds, J. Rhodes, M. Rhodes, M. C. Richardson, B. Rice, N. G. Rice, R. Rieben, A. Rigatti, S. Riggs, H. G. Rinderknecht, K. Ring, B. Riordan, R. Riquier, C. Rivers, D. Roberts, V. Roberts, G. Robertson, H. F. Robey, J. Robles, P. Rocha, G. Rochau, J. Rodriguez, S. Rodriguez, M. Rosen, M. Rosenberg, G. Ross, J. S. Ross, P. Ross, J. Rouse, D. Rovang, A. M. Rubenchik, M. S. Rubery, C. L. Ruiz, M. Rushford, B. Russ, J. R. Rygg, B. S. Ryujin, R. A. Sacks, R. F. Sacks, K. Saito, T. Salmon, J. D. Salmonson, J. Sanchez, S. Samuelson, M. Sanchez, C. Sangster, A. Saroyan, J. Sater, A. Satsangi, S. Sauers, R. Saunders, J. P. Sauppe, R. Sawicki, D. Sayre, M. Scanlan, K. Schaffers, G. T. Schappert, S. Schiaffino, D. J. Schlossberg, D. W. Schmidt, M. J. Schmitt, D. H. G. Schneider, M. B. Schneider, R. Schneider, M. Schoff, M. Schollmeier, M. Scholmerich, C. R. Schroeder, S. E. Schrauth, H. A. Scott, I. Scott, J. M. Scott, R. H. H. Scott, C. R. Scullard, T. Sedillo, F. H. Seguin, W. Seka, J. Senecal, S. M. Sepke, L. Seppala, K. Sequoia, J. Severyn, J. M. Sevier, N. Sewell, S. Seznec, R. C. Shah, J. Shamlian, D. Shaughnessy, M. Shaw, R. Shaw, C. Shearer, R. Shelton, N. Shen, M. W. Sherlock, A. I. Shestakov, E. L. Shi, S. J. Shin, N. Shingleton, W. Shmayda, M. Shor, M. Shoup, C. Shuldberg, L. Siegel, F. J. Silva, A. N. Simakov, B. T. Sims, D. Sinars, P. Singh, H. Sio, K. Skulina, S. Skupsky, S. Slutz, M. Sluyter, V. A. Smalyuk, D. Smauley, R. M. Smeltser, C. Smith, I. Smith, J. Smith, L. Smith, R. Smith, R. Sohn, S. Sommer, C. Sorce, M. Sorem, J. M. Soures, M. L. Spaeth, B. K. Spears, S. Speas, D. Speck, R. Speck, J. Spears, T. Spinka, P. T. Springer, M. Stadermann, B. Stahl, J. Stahoviak, L. G. Stanton, R. Steele, W. Steele, D. Steinman, R. Stemke, R. Stephens, S. Sterbenz, P. Sterne, D. Stevens, J. Stevers, C. B. Still, C. Stoeckl, W. Stoeffl, J. S. Stolken, C. Stolz, E. Storm, G. Stone, S. Stoupin, E. Stout, I. Stowers, R. Strauser, H. Streckart, J. Streit, D. J. Strozzi, T. Suratwala, G. Sutcliffe, L. J. Suter, S. B. Sutton, V. Svidzinski, G. Swadling, W. Sweet, A. Szoke, M. Tabak, M. Takagi, A. Tambazidis, V. Tang, M. Taranowski, L. A. Taylor, S. Telford,

W. Theobald, M. Thi, A. Thomas, C. A. Thomas, I. Thomas, R. Thomas, I. J. Thompson, A. Thongstisubskul, C. B. Thorsness, G. Tietbohl, R. E. Tipton, M. Tobin, N. Tomlin, R. Tommasini, A. J. Toreja, J. Torres, R. P. J. Town, S. Townsend, J. Trenholme, A. Trivelpiece, C. Trosseille, H. Truax, D. Trummer, S. Trummer, T. Truong, D. Tubbs, E. R. Tubman, T. Tunnell, D. Turnbull, R. E. Turner, M. Ulitsky, R. Upadhye, J. L. Vaher, P. VanArsdall, D. VanBlarcom, M. Vandenboomgaerde, R. VanQuinlan, B. M. Van Wonterghem, W. S. Varnum, A. L. Velikovich, A. Vella, C. P. Verdon, B. Vermillion, S. Vernon, R. Vesey, J. Vickers, R. M. Vignes, M. Visosky, J. Vocke, P. L. Volegov, S. Vonhof, R. Von Rotz, H. X. Vu, M. Vu, D. Wall, J. Wall, R. Wallace, B. Wallin, D. Walmer, C. A. Walsh, C. F. Walters, C. Waltz, A. Wan, A. Wang, Y. Wang, J. S. Wark, B. E. Warner, J. Watson, R. G. Watt, P. Watts, J. Weaver, R. P. Weaver, S. Weaver, C. R. Weber, P. Weber, S. V. Weber, P. Wegner, B. Welday, L. Welser-Sherrill, K. Weiss, K. Widmann, G. F. Wheeler, W. Whistler, R. K. White, H. D. Whitley, P. Whitman, M. E. Wickett, C. Widmayer, J. Wiedwald, R. Wilcox, S. Wilcox, C. Wild, B. H. Wilde, C. H. Wilde, K. Wilhelmsen, M. D. Wilke, H. Wilkens, P. Wilkins, S. C. Wilks, E. A. Williams, G. J. Williams, W. Williams, W. H. Williams, D. C. Wilson, B. Wilson, E. Wilson, R. Wilson, S. Winters, J. Wisoff, M. Wittman, J. Wolfe, A. Wong, K. W. Wong, L. Wong, N. Wong, R. Wood, D. Woodhouse, J. Woodruff, D. T. Woods, S. Woods, B. N. Woodworth, E. Wooten, A. Wootton, K. Work, J. B. Workman, J. Wright, M. Wu, C. Wuest, F. J. Wysocki, H. Xu, M. Yamaguchi, B. Yang, S. T. Yang, J. Yatabe, C. B. Yeamans, B. C. Yee, S. A. Yi, L. Yin, B. Young, C. S. Young, C. V. Young, P. Young, K. Youngblood, R. Zacharias, G. Zagaris, N. Zaitseva, F. Zaka, F. Ze, B. Zeiger, M. Zika, G. B. Zimmerman, T. Zobrist, J. D. Zuegel, A. B. Zylstra and I. C. F. C. Indirect Drive, Phys Rev Lett **129** (7), 075001 (2022).

60. V. N. Goncharov, T. C. Sangster, R. Betti, T. R. Boehly, M. J. Bonino, T. J. B. Collins, R. S. Craxton, J. A. Delettrez, D. H. Edgell, R. Epstein, R. K. Follett, C. J. Forrest, D. H. Froula, V. Yu. Glebov, D. R. Harding, R. J. Henchen, S. X. Hu, I. V. Igumenshchev, R. Janezic, J. H. Kelly, T. J. Kessler, T. Z. Kosc, S. J. Loucks, J. A. Marozas, F. J. Marshall, A. V. Maximov, R. L. McCrory, P. W. McKenty, D. D. Meyerhofer, D. T. Michel, J. F. Myatt, R. Nora, P. B. Radha, S. P. Regan, W. Seka, W. T. Shmayda, R. W. Short, A. Shvydky, S. Skupsky, C. Stoeckl, B. Yaakobi, J. A. Frenje, M. Gatu-Johnson, R. D. Petrasso and D. T. Casey, Phys. Plasmas **21**, 56315 (2014).

61. H. F. Robey, P. M. Celliers, J. L. Kline, A. J. Mackinnon, T. R. Boehly, O. L. Landen, J. H. Eggert, D. Hicks, S. Le Pape, D. R. Farley, M. W. Bowers, K. G. Krauter, D. H. Munro, O. S. Jones, J. L. Milovich, D. Clark, B. K. Spears, R. P. Town, S. W. Haan, S. Dixit, M. B. Schneider, E. L. Dewald, K. Widmann, J. D. Moody, T. D. Doppner, H. B. Radousky, A. Nikroo, J. J. Kroll, A. V. Hamza, J. B. Horner, S. D. Bhandarkar, E. Dzenitis, E. Alger, E. Giraldez, C. Castro, K. Moreno, C. Haynam, K. N. LaFortune, C. Widmayer, M. Shaw, K. Jancaitis, T. Parham, D. M. Holunga, C. F. Walters, B. Haid, T. Malsbury, D. Trummer, K. R. Coffee, B. Burr, L. V. Berzins, C. Choate, S. J. Brereton, S. Azevedo, H. Chandrasekaran, S. Glenzer, J. A. Caggiano, J. P. Knauer, J. A. Frenje, D. T. Casey, M. G. Johnson, F. H. Seguin, B. K. Young, M. J. Edwards, B. M. Van Wonterghem, J. Kilkenny, B. J. MacGowan, J. Atherton, J. D. Lindl, D. D. Meyerhofer and E. Moses, Phys Rev Lett **108** (21), 215004 (2012).

62. O. L. L. Landen, R. Benedetti, D. Bleuel, T. R. R. Boehly, D. K. K. Bradley, J. A. A. Caggiano, D. A. A. Callahan, P. M. M. Celliers, C. J. J. Cerjan, D. Clark, G. W. W. Collins, E. L. L. Dewald, S. N. N. Dixit, T. Doeppner, D. Edgell, J. Eggert, D. Farley, J. A. A. Frenje, V. Glebov, S. M. M. Glenn, S. H. H. Glenzer, S. W. W. Haan, A. Hamza, B. A. A. Hammel, C. A. A. Haynam, J. H. H. Hammer, R. F. F. Heeter, H. W. W. Herrmann, D. G. G. Hicks, D. E. E. Hinkel, N. Izumi,

M. Gatu Johnson, O. S. S. Jones, D. H. H. Kalantar, R. L. L. Kauffman, J. D. D. Kilkenny, J. L. L. Kline, J. P. P. Knauer, J. A. A. Koch, G. A. A. Kyrala, K. Lafortune, T. Ma, A. J. J. MacKinnon, A. J. J. MacPhee, E. Mapoles, J. L. L. Milovich, J. D. D. Moody, N. B. B. Meezan, P. Michel, A. S. S. Moore, D. H. H. Munro, A. Nikroo, R. E. E. Olson, K. Opachich, A. Pak, T. Parham, P. Patel, H.-S. S. Park, R. P. P. Petrasso, J. Ralph, S. P. P. Regan, B. A. A. Remington, H. G. G. Rinderknecht, H. F. F. Robey, M. D. D. Rosen, J. S. S. Ross, J. D. D. Salmonson, T. C. C. Sangster, M. B. B. Schneider, V. Smalyuk, B. K. K. Spears, P. T. T. Springer, L. J. J. Suter, C. A. A. Thomas, R. P. J. P. J. Town, S. V. V. Weber, P. J. J. Wegner, D. C. C. Wilson, K. Widmann, C. Yeamans, A. Zylstra, M. J. J. Edwards, J. D. D. Lindl, L. J. J. Atherton, W. W. W. Hsing, B. J. J. MacGowan, B. M. M. Van Wonterghem, E. I. I. Moses, others, R. Benedetti, D. Bleuel, T. R. R. Boehly, D. K. K. Bradley, J. A. A. Caggiano, D. A. A. Callahan, P. M. M. Celliers, C. J. J. Cerjan, D. Clark, G. W. W. Collins, E. L. L. Dewald, S. N. N. Dixit, T. Döppner, D. Edgell, J. Eggert, D. Farley, J. A. A. Frenje, V. Glebov, S. M. M. Glenn, S. H. H. Glenzer, S. W. W. Haan, A. Hamza, B. A. A. Hammel, C. A. A. Haynam, J. H. H. Hammer, R. F. F. Heeter, H. W. W. Herrmann, D. G. G. Hicks, D. E. E. Hinkel, N. Izumi, M. Gatu Johnson, O. S. S. Jones, D. H. H. Kalantar, R. L. L. Kauffman, J. D. D. Kilkenny, J. L. L. Kline, J. P. P. Knauer, J. A. A. Koch, G. A. A. Kyrala, K. Lafortune, T. Ma, A. J. J. MacKinnon, A. J. J. MacPhee, E. Mapoles, J. L. L. Milovich, J. D. D. Moody, N. B. B. Meezan, P. Michel, A. S. S. Moore, D. H. H. Munro, A. Nikroo, R. E. E. Olson, K. Opachich, A. Pak, T. Parham, P. Patel, H.-S. S. Park, R. P. P. Petrasso, J. Ralph, S. P. P. Regan, B. A. A. Remington, H. G. G. Rinderknecht, H. F. F. Robey, M. D. D. Rosen, J. S. S. Ross, J. D. D. Salmonson, T. C. C. Sangster, M. B. B. Schneider, V. Smalyuk, B. K. K. Spears, P. T. T. Springer, L. J. J. Suter, C. A. A. Thomas, R. P. J. P. J. Town, S. V. V. Weber, P. J. J. Wegner, D. C. C. Wilson, K. Widmann, C. Yeamans, A. Zylstra, M. J. J. Edwards, J. D. D. Lindl, L. J. J.

Atherton, W. W. W. Hsing, B. J. J. MacGowan, B. M. M. Van Wonterghem and E. I. I. Moses, Plasma Physics and Controlled Fusion **54**, 124026 (2012).

63. O. A. Hurricane and others, Physics of Plasmas **29**, 12703 (2022).

64. D. T. Casey, O. L. Landen, E. Hartouni, R. M. Bionta, K. D. Hahn, P. L. Volegov, D. N. Fittinghoff, V. Geppert-Kleinrath, C. H. Wilde, J. L. Milovich, V. A. Smalyuk, J. E. Field, O. A. Hurricane, A. B. Zylstra, A. L. Kritcher, D. S. Clark, C. V. Young, R. C. Nora, D. A. Callahan, B. J. MacGowan, D. H. Munro, B. K. Spears, J. L. Peterson, J. A. Gaffney, K. D. Humbird, M. K. G. Kruse, A. S. Moore, D. J. Schlossberg, M. Gatu-Johnson and J. A. Frenje, Physics of Plasmas **28** (4) (2021).

65. O. L. Landen, D. T. Casey, J. M. DiNicola, T. Doeppner, E. P. Hartouni, D. E. Hinkel, L. F. Berzak Hopkins, M. Hohenberger, A. L. Kritcher, S. LePape, B. J. MacGowan, S. Maclaren, K. D. Meaney, M. Millot, P. K. Patel, J. Park, L. A. Pickworth, H. F. Robey, J. S. Ross, S. T. Yang, A. B. Zylstra, K. L. Baker, D. A. Callahan, P. M. Celliers, M. J. Edwards, O. A. Hurricane, J. D. Lindl, J. D. Moody, J. Ralph, V. A. Smalyuk, C. A. Thomas, B. M. Van Wonterghem and C. R. Weber, High Energy Density Physics **36**, 100765 (2020).

66. T. Döppner, D. A. Callahan, O. A. Hurricane, D. E. Hinkel, T. Ma, H. S. Park, L. F. Berzak Hopkins, D. T. Casey, P. Celliers, E. L. Dewald, T. R. Dittrich, S. W. Haan, A. L. Kritcher, A. MacPhee, S. Le Pape, A. Pak, P. K. Patel, P. T. Springer, J. D. Salmonson, R. Tommasini, L. R. Benedetti, E. Bond, D. K. Bradley, J. Caggiano, J. Church, S. Dixit, D. Edgell, M. J. Edwards, D. N. Fittinghoff, J. Frenje, M. Gatu Johnson, G. Grim, R. Hatarik, M. Havre, H. Herrmann, N. Izumi, S. F. Khan, J. L. Kline, J. Knauer, G. A. Kyrala, O. L. Landen, F. E. Merrill, J. Moody, A. S. Moore, A. Nikroo, J. E. Ralph, B. A. Remington, H. F. Robey, D. Sayre, M. Schneider, H.

Streckert, R. Town, D. Turnbull, P. L. Volegov, A. Wan, K. Widmann, C. H. Wilde and C. Yeamans, Phys Rev Lett **115** (5), 055001 (2015).

67. P. Amendt, D. Ho, Y. Ping, V. Smalyuk, S. Khan, J. Lindl, D. Strozzi, R. Tommasini, M. Belyaev, C. Cerjan, O. Jones, W. Kruer, N. Meezan, H. Robey, F. Tsung, C. Weber and C. Young, Physics of Plasmas **26** (8), 082707 (2019).

68. D. E. Hinkel, L. F. Berzak Hopkins, T. Ma, J. E. Ralph, F. Albert, L. R. Benedetti, P. M. Celliers, T. Doppner, C. S. Goyon, N. Izumi, L. C. Jarrott, S. F. Khan, J. L. Kline, A. L. Kritcher, G. A. Kyrala, S. R. Nagel, A. E. Pak, P. Patel, M. D. Rosen, J. R. Rygg, M. B. Schneider, D. P. Turnbull, C. B. Yeamans, D. A. Callahan and O. A. Hurricane, Phys Rev Lett **117** (22), 225002 (2016).

69. A. L. Kritcher, C. Young, H. F. Robey and others, Nature Physics (2022).

70. K. L. Baker, (Lawrence Livermore National Laboratory, 2022).

71. L. Berzak Hopkins, L. Divol, C. Weber, S. Le Pape, N. B. Meezan, J. S. Ross, R. Tommasini, S. Khan, D. D. Ho, J. Biener, E. Dewald, C. Goyon, C. Kong, A. Nikroo, A. Pak, N. Rice, M. Stadermann, C. Wild, D. Callahan and O. Hurricane, Physics of Plasmas **25** (8) (2018).

FIGURE CAPTIONS

Figure 1 a) Pulse shapes, b) ablator remaining mass and coast times and c) peak fuel implosion velocity for the simulations performed for [1].

Figure 2 Hot spot pressure versus peak power for BigFoot data (green points) and simulations (black points). Overplotted curve Is analytic scaling valid for pressures below 400 Gbar.

Figure 3 Pulse shape for 400 TW N190721 and extrapolation to a 500 TW design to maintain ~ constant percentage mass remaining.

Figure 4 Yield amplifications, Y_{amp}, as a function of a) laser energy and b) capsule absorbed energy for numerous campaigns conducted on the NIF.

Figure 5 Yield amplification, Y_{amp}, as a function of laser energy for the four BigFoot layered implosions(green circles) carried out in the 5.4 by 10.13 mm size hohlraum, and simulations[1] (black circles) which extrapolate the performance to higher laser energies. The neutron-based hotspot shapes measured in each of the experiments are plotted next to inferred yield

amplifications. Also included are the two Iraum, brown circles, and HyE 1050, gray circles, shots which recently crossed the burning plasma threshold with 400 to 500 kJ more effective energy.

Figure 6 Yield amplification versus no-alpha GLC from 1D full-scale Bigfoot simulations (black) on which is overplotted measured Y_{amp} of N190721 (green point) and 500 TW design at $\sqrt{}$GLC = $\sqrt{}$3 higher per Table 3 (red point).

Figure 7 Down-scattered ratio, DSR, vs. initial ice thickness for most campaigns on the NIF. A) The point size is proportional to the percent of dopant in the ablator, W dopant for the HDC ablator campaigns(BF, HDC, Iraum, HyB, HyE1100 and HyE1050) and Si for the CH ablator campaigns(LF, HF, ASHF and HF low fill). B) The point size is proportional to the coast time of the implosion.

Table 1 Simulated hotspot variables used to calculate the hotspot pressure and yield amplifications for BigFoot 844 designs as increase laser peak power and energy.

Table 2 Measured data from the BigFoot 844 campaigns.

Table 3 Input and output parameters for 400 TW N190721 and analytic extrapolations to 500 TW under various constraints.

FIGURES

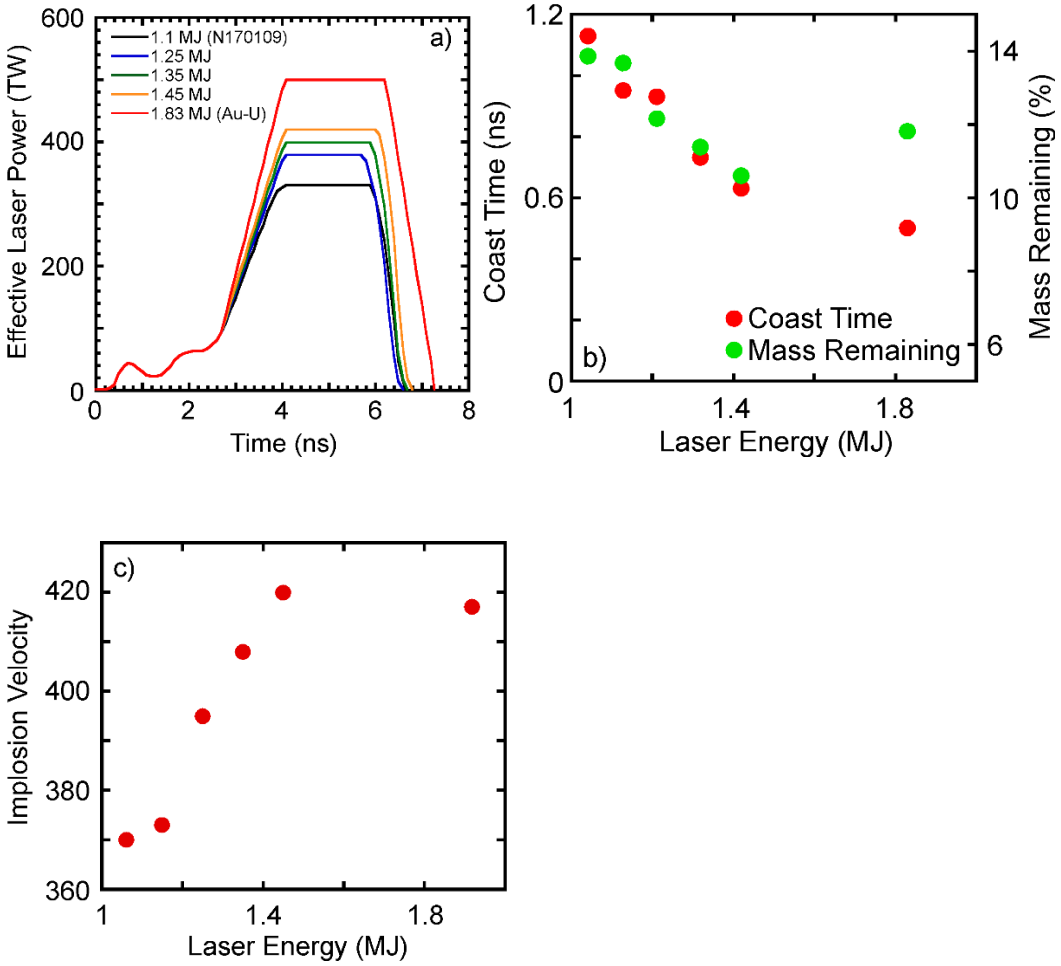

Figure 1

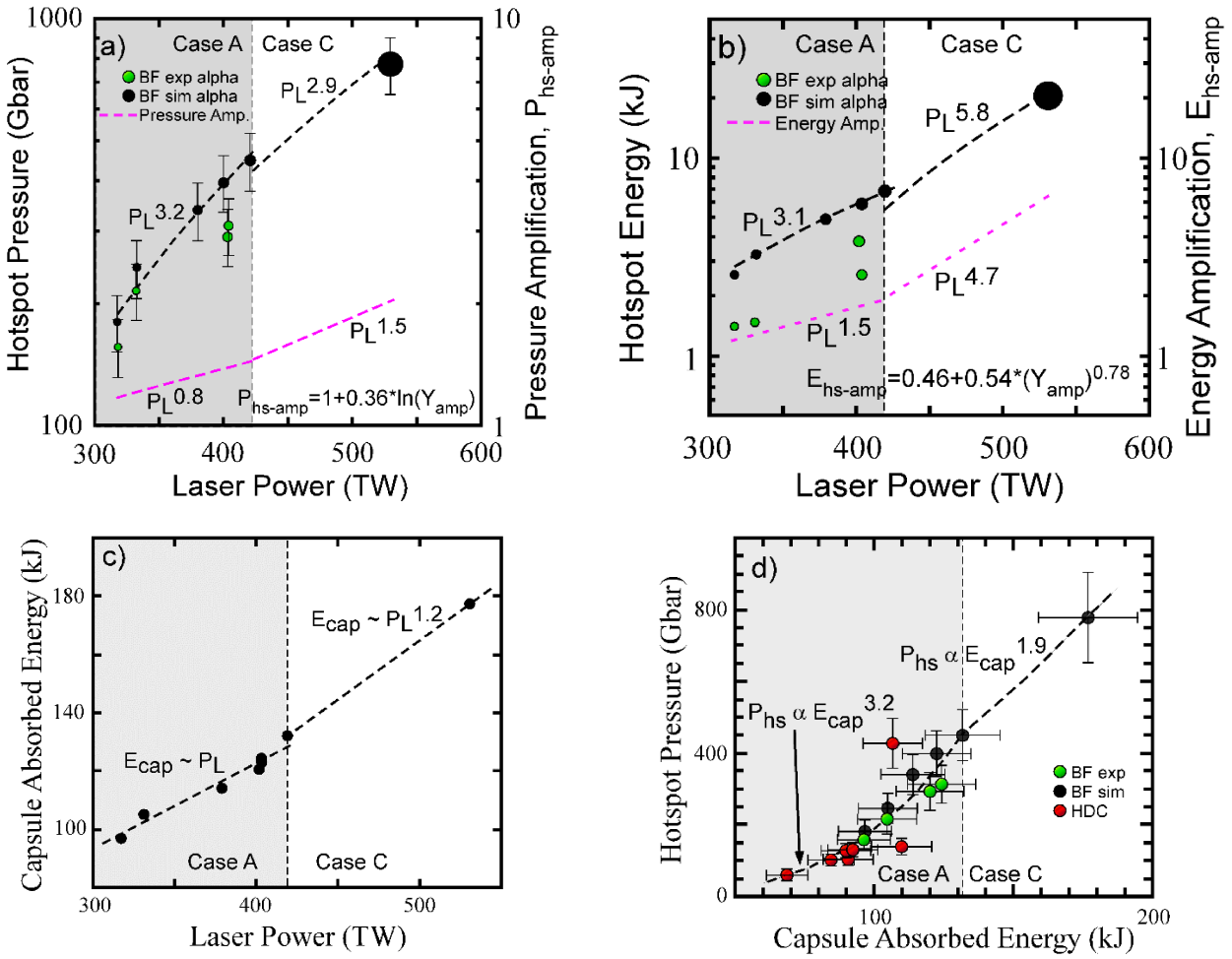
a)
Case A
Case C
BF exp alpha
BF sim alpha
Pressure Amp.
$P_L^{2.9}$
$P_L^{3.2}$
$P_L^{1.5}$
$P_L^{0.8}$
$P_{hs\text{-}amp}$=1+0.36*ln(Y_{amp})
Hotspot Pressure (Gbar)
Pressure Amplification, $P_{hs\text{-}amp}$
Laser Power (TW)
b)
Case A
Case C
BF exp alpha
BF sim alpha
Energy Amp
$P_L^{5.8}$
$P_L^{3.1}$
$P_L^{4.7}$
$P_L^{1.5}$
$E_{hs\text{-}amp}$=0.46+0.54*(Y_{amp})$^{0.78}$
Hotspot Energy (kJ)
Energy Amplification, $E_{hs\text{-}amp}$
Laser Power (TW)
c)
$E_{cap} \sim P_L^{1.2}$
$E_{cap} \sim P_L$
Case A
Case C
Capsule Absorbed Energy (kJ)
Laser Power (TW)
d)
$P_{hs} \alpha E_{cap}^{1.9}$
$P_{hs} \alpha E_{cap}^{3.2}$
BF exp
BF sim
HDC
Case A
Case C
Hotspot Pressure (Gbar)
Capsule Absorbed Energy (kJ)

Figure 2

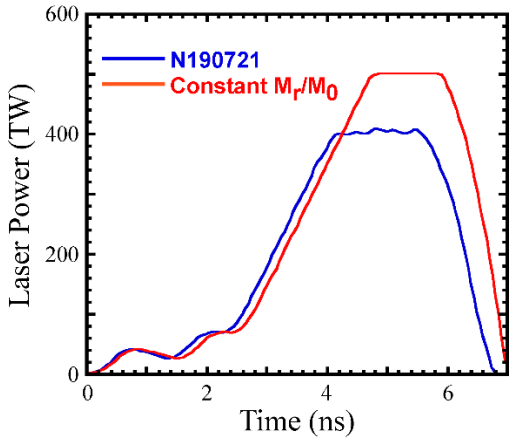
600
400
200
0
Laser Power (TW)
0
2
4
6
Time (ns)
N190721
Constant M_r/M_0

Figure 3

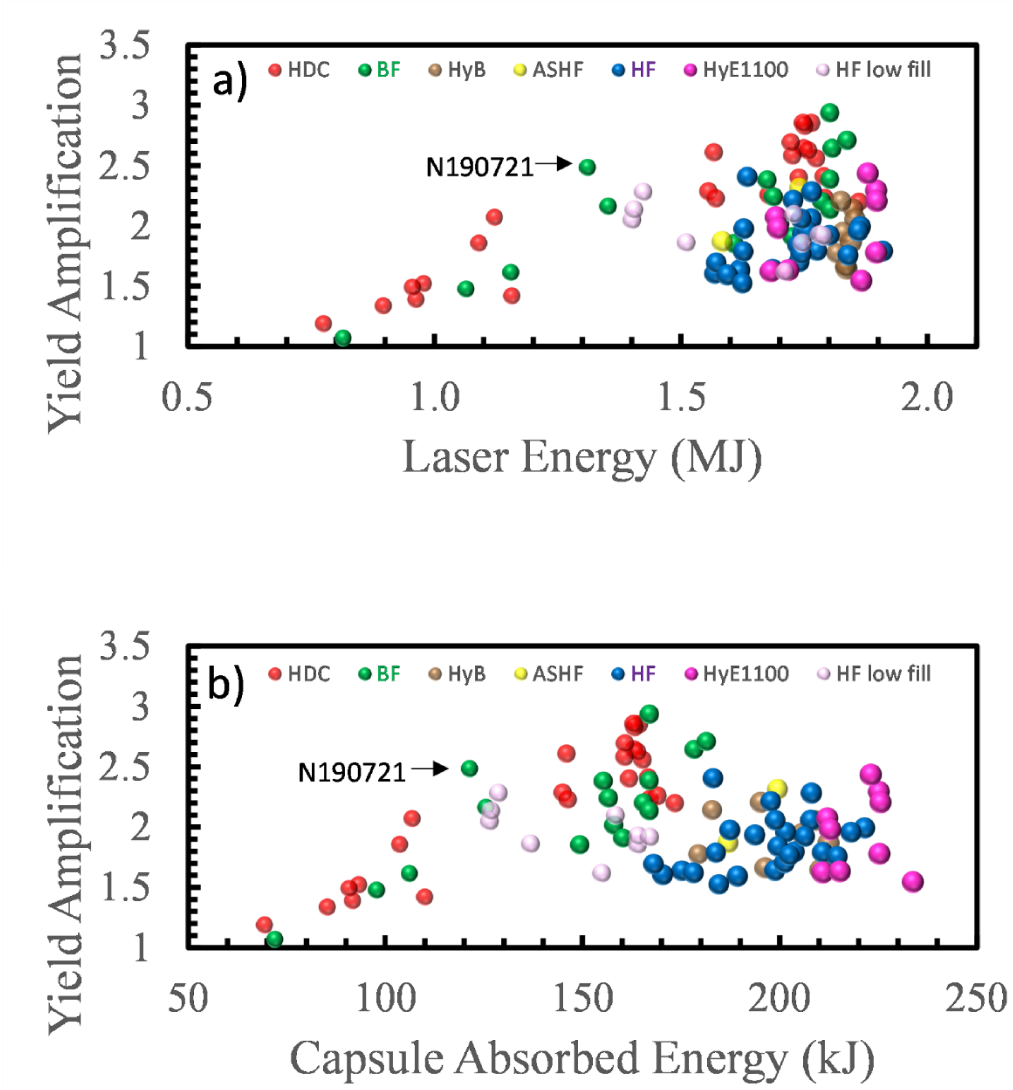
a)
HDC
BF
HyB
ASHF
HF
HyE1100
HF low fill
N190721
Yield Amplification
Laser Energy (MJ)
3.5
3
2.5
2
1.5
1
0.5
1.0
1.5
2.0
b)
HDC
BF
HyB
ASHF
HF
HyE1100
HF low fill
N190721
Yield Amplification
Capsule Absorbed Energy (kJ)
50
100
150
200
250

Figure 4

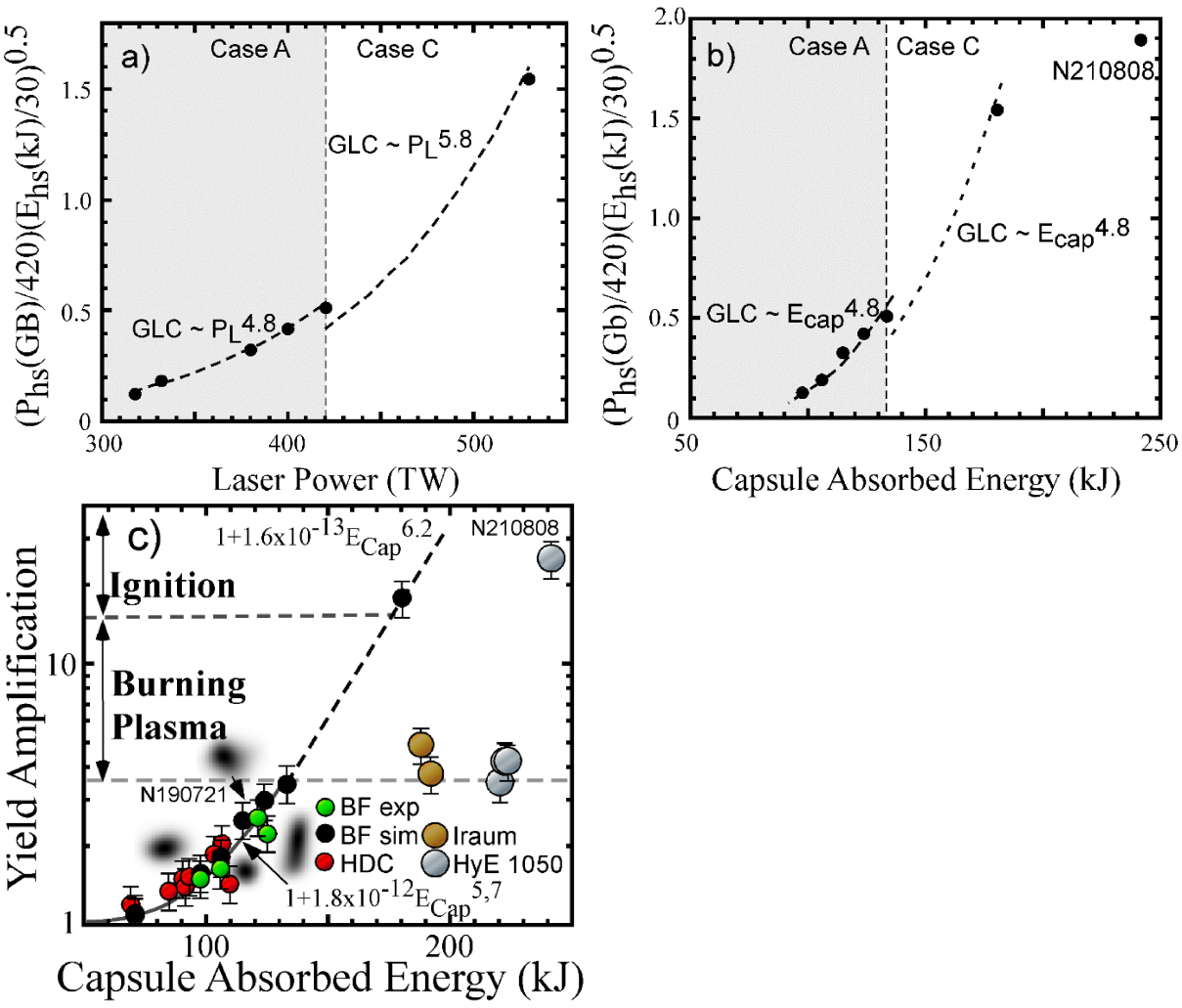
a)
Case A
Case C
GLC ~ P_L^5.8
GLC ~ P_L^4.8
(P_hs(GB)/420)(E_hs(kJ)/30)^0.5
Laser Power (TW)
b)
Case A
Case C
N210808
GLC ~ E_cap^4.8
GLC ~ E_cap^4.8
(P_hs(Gb)/420)(E_hs(kJ)/30)^0.5
Capsule Absorbed Energy (kJ)
c)
1+1.6x10^-13 E_Cap^6.2
N210808
Ignition
Burning Plasma
N190721
BF exp
BF sim
HDC
Iraum
HyE 1050
1+1.8x10^-12 E_Cap^5.7
Yield Amplification
Capsule Absorbed Energy (kJ)

Figure 5

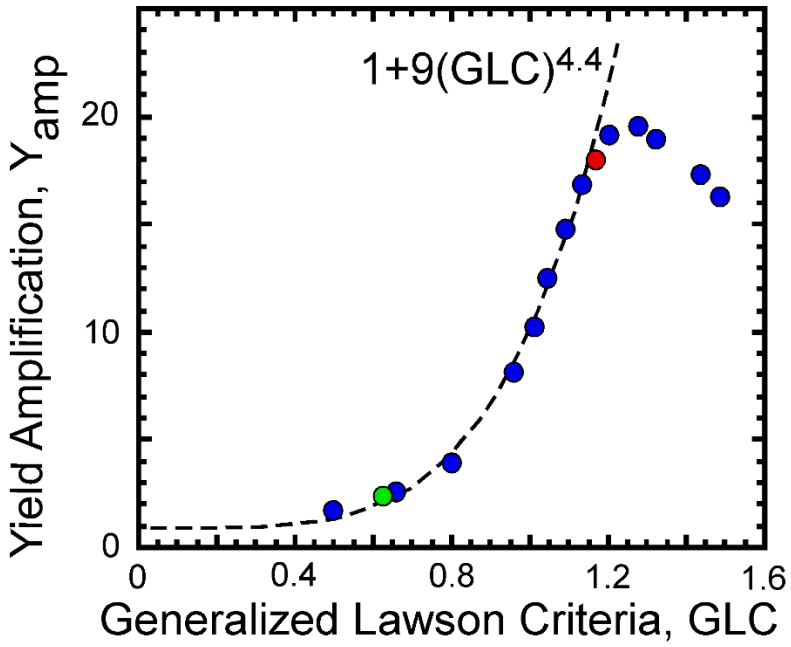
1+9(GLC)^4.4
Yield Amplification, Y_amp
Generalized Lawson Criteria, GLC
0
10
20
0
0.4
0.8
1.2
1.6

Figure 6

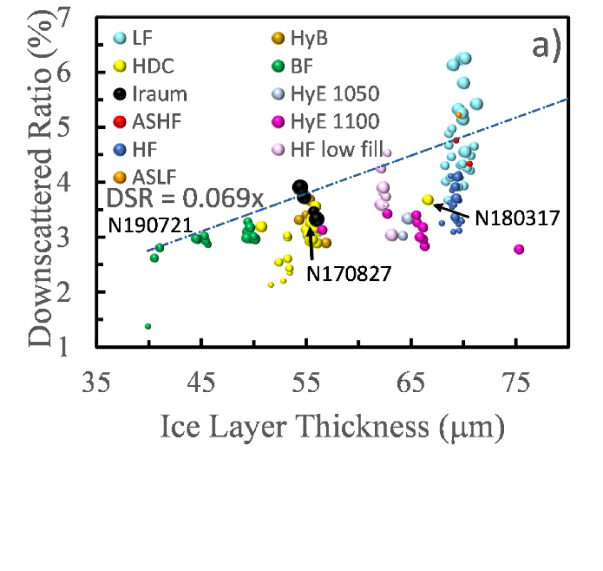
a)
LF
HDC
Iraum
ASHF
HF
ASLF
HyB
BF
HyE 1050
HyE 1100
HF low fill
DSR = 0.069x
N190721
N170827
N180317
Downscattered Ratio (%)
Ice Layer Thickness (µm)
1
2
3
4
5
6
7
35
45
55
65
75

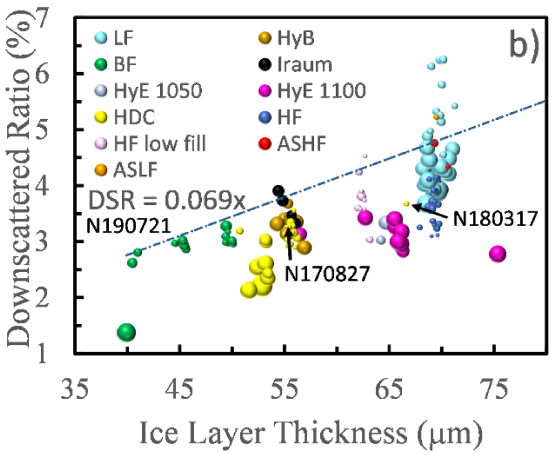
b)
LF
BF
HyE 1050
HDC
HF low fill
ASLF
HyB
Iraum
HyE 1100
HF
ASHF
DSR = 0.069x
N190721
N170827
N180317
Downscattered Ratio (%)
Ice Layer Thickness (µm)
1
2
3
4
5
6
7
35
45
55
65
75

Figure 7

Sim. Results	Laser Energy (MJ)	Laser Power (TW)	Ablator thickness (μm)	DT fuel thickness (μm)	Peak implosion velocity (μm/ns)	Ablator Mass Rem. (%)	Coast Time (ns)	Primary yield	Ion Temp. (keV)	DSR (%)	Hotspot Pressure (Gbar)	Y_{amp}
N161030	1.06	318	63.8	40.4	370	9.8	1.13	$2.1x10^{15}$	3.91	2.68	180	1.6
N170109	1.15	332	63.8	41	372	9.6	1.07	$3.7x10^{15}$	4.06	2.79	244	1.8
X1	1.25	380	63.8	40	395	8.0	0.93	$8.6x10^{15}$	4.67	2.97	338	2.6
X2	1.35	400	63.8	40	409	7.3	0.73	$1.2x10^{16}$	5.03	3.02	395	3.1
X3	1.45	420	63.8	40	421	6.5	0..63	$1.6x10^{16}$	5.51	3.04	449	3.6
X4	1.9	500	76.6	48	417	8.4	0.5	$9.6x10^{16}$	7.56	3.5	775	21

Table 1

Shot or Design	Laser Energy (MJ)	Laser Power (TW)	Ablator thickness (um)	DT Fuel thickness (um)	Peak velocity (μm/ns)	Primary yield	Tion (keV)	DSR (%)	Neutron P0 (μm)	Hotspot Pressure (Gbar)	Yield Amp.
N161030	1.06	318	63.8	39.9	388	$1.7 x10^{15}$	4.14	2.61	24.4	158	1.5
N170109	1.15	332	65.3	40.5	392	$2.3 x10^{15}$	4.16	2.81	22.4	214	1.6
N190617	1.35	404	68.5	41.0	404	$6.6 x10^{15}$	4.58	3.12	22.3	316	2.2
N190721	1.31	403	68.3	44.6	400	$9.5 x10^{15}$	4.83	3.12	27.6	291	2.5

Table 2

Shot or Design	Eff Laser Power (TW)	Peak power duration (ns)	Laser Energy (MJ)	Peak T_r (eV)	Ablator thickness (μm)	DT Fuel thickness (μm)	v_{imp} (μm/ns)	M_r/M (%)	EP^2 (norm)
N190721	400	2.1	1.3	300	68	45	400	12	1
Fixed M	500	1.75	1.35	320	68	45	480	8	4.2
Fixed M_r	500	1.9	1.5	320	76	45	437	10.7	2.8
Fixed v_{imp}	500	2.1	1.6	320	82	45	400	12.8	2.4
Fixed M_r DU	530	1.9	1.6	325	78	45	446	10.4	3.6

Table 3